Applied Energy 210 (2018) 351–375

Contents lists available at ScienceDirect

Applied Energy

journal homepage: www.elsevier.com/locate/apenergy

Numerical and experimental evaluation and optimization of ceramic foam as solar absorber – Single-layer vs multi-layer configurations

Fritz Zaversky[a,*], Leticia Aldaz[a], Marcelino Sánchez[a], Antonio L. Ávila-Marín[b], M. Isabel Roldán[c], Jesús Fernández-Reche[c], Alexander Füssel[d], Wieland Beckert[d], Jörg Adler[d]

[a] National Renewable Energy Center (CENER), Solar Thermal Energy Department, c/Ciudad de la Innovación 7, Sarriguren, Navarre, Spain
[b] CIEMAT – Plataforma Solar de Almería, Avda. Complutense 40, Madrid E-28040, Spain
[c] CIEMAT – Plataforma Solar de Almería, P.O. Box 22, Tabernas-Almeria E-04200, Spain
[d] Fraunhofer-Institut für Keramische Technologien und Systeme IKTS, Winterbergstr. 28, 01277 Dresden, Germany

HIGHLIGHTS

- The thermal efficiency of ceramic foam absorbers depends strongly on their porosity.
- The highest possible porosity should be chosen for future solar receiver designs.
- A flat efficiency maximum can be observed for cell densities between 30 and 50 PPI.
- An optimized single-layer configuration is the absorber of choice.
- Multi-layer configurations do not have any advantage regarding thermal performance.

ARTICLE INFO

Keywords:
Concentrated solar power (CSP)
Ceramic foam absorber
Optimization
1-D modeling

ABSTRACT

This work targets the numerical and experimental evaluation of ceramic foam as solar absorber material for solar thermal power generation. Two different 1-D model types with local thermal non-equilibrium (LTNE) have been developed independently at CENER and Fraunhofer-IKTS. The modeling of radiation propagation inside the foam is considered via two approaches. One approach is based on a discrete-ordinate solution of the radiation transport equation; the other imposes the solar flux defining an exponential attenuation, as derived from Bouguer's law, and considering thermal radiation transport according to Rosseland's diffusion approximation.

Both models have been successfully checked for consistency against experimental data obtained at a 4 kW solar simulator. Then, the models have been run applying automatic scripts, performing a large number of parameter variations, optimizing for the absorber thermal efficiency. It is important to note that single, double and triple layer absorber configurations have been studied, since previous works found that a decreasing porosity in direction of flow can enhance absorber performance.

The parametric optimization studies have shown that the porosity of the foam is strongly related to the obtained thermal efficiency. The higher the porosity of the foam, the higher is also the absorber thermal efficiency. A broad plateau-like efficiency maximum can be observed for cell densities between 30 and 50 PPI (pores per inch). When applying a multi-layer configuration, no significant correlation can be observed between efficiency and the properties of the second or third layer. Only the parameters of the first layer seem to determine the thermal performance. This leads to the conclusion that an optimized single-layer configuration is the absorber of choice. If necessary, a second layer could be applied to satisfy mechanical stability aspects.

1. Introduction

Solar thermal power, also known as concentrated solar power (CSP) or solar thermal electricity (STE), is a renewable energy sector with great potential, as it directly harnesses the abundant amount of solar energy incident on planet earth. CSP plants capture the sun's direct normal irradiation (DNI), concentrate it onto a receiving surface, and transform the absorbed heat into mechanical work and subsequently, into electric energy by using state-of-the-art thermodynamic power cycles. Unlike other renewable energy sectors (such as wind or

* Corresponding author.
E-mail addresses: fzaversky@cener.com, fritz.zaversky@alumni.tugraz.at (F. Zaversky).

https://doi.org/10.1016/j.apenergy.2017.11.003
Received 3 August 2017; Received in revised form 28 September 2017; Accepted 1 November 2017
Available online 09 November 2017

Nomenclature

A	area (m^2)
$A_{surface}$	surface area for convective heat transfer (m^2)
$A_{receiver}$	aperture area of receiver (m^2)
d_c	cell diameter (m)
d_h	hydraulic diameter of foam (m)
d_w	window diameter (m)
Hg	Hagen number (–)
h_{abs}	absorber thickness (m)
$h_{ambient}$	convective heat transfer coefficient between ambient air and receiver front face ($W/(m^2 K)$)
$h_{a,i}$	upstream specific enthalpy at the left boundary of control volume i (J/kg)
$h_{b,i}$	upstream specific enthalpy at the right boundary of control volume i (J/kg)
h_{fi}	convective interstitial heat transfer coefficient between solid and fluid at node i ($W/(m^2 K)$)
h_i	specific enthalpy of control volume i (J/kg)
h_v	convective volumetric heat transfer coefficient between solid and fluid ($W/(m^3 K)$)
I_0	solar flux incident on the absorber's front face (W/m^2)
I_i	solar flux incident at node i (W/m^2)
K	extinction coefficient (m^{-1})
k_f	thermal conductivity of fluid (W/(m K))
k_{eff}	effective thermal conductivity (W/(m K))
k_{con}	conductive contribution of effective conductivity (W/(m K))
k_{rad}	radiative contribution of effective conductivity (W/(m K))
k_s	pure solid thermal conductivity (W/(m K))
l	edge length of tetrakaidecahedron – idealized cell geometry (m)
m_i	total fluid mass inside the control volume i (kg)
$\dot{m}_{a,i}$	mass flow at left boundary of control volume i, if entering positive else negative (kg/s)
$\dot{m}_{b,i}$	mass flow at right boundary of control volume i, if leaving positive else negative (kg/s)
Nu	Nusselt number (–)
p_i	pressure within control volume i (Pa)
q	total radiative flow in Discrete Ordinate Model (W/m^2)
$q_{in,sol}$	incident solar radiation flow in Discrete Ordinate Model (W/m^2)
$\dot{Q}_{con}$	convective heat loss from absorber front surface (W)
$\dot{Q}_{net,\,i}$	net heat flow over the control volume i boundary (W)
$\dot{Q}_{rad}$	radiative heat loss from absorber front face (W)
$\dot{Q}_{rad,V}$	volumetric radiative thermal heat source in Discrete Ordinate Model (W/m^2)
R_i	area ratio at node section i (–)
s	radiation path position variable in Discrete Ordinate Model (m)
S_v	specific surface area (m^2/m^3)
T	temperature (K)
$T_{env,in/out}$	ambient temperature at absorber inlet, resp. outlet side (K)
T_{si}	solid temperature at node i (K)
t	time (s)
t_s	strut thickness (m)
U_i	total internal energy of control volume i (J)
u_i	specific internal energy of control volume i (J/kg)
V_i	total volume of the control volume i (m^3)
v_i	flow velocity within control volume i (m/s)
v_s	superficial flow velocity – empty tube velocity (m/s)
v	interstitial velocity (m/s)
z	coordinate in direction of air flow, absorber depth (m)
Δp	pressure drop (Pa)
ΔL	flow length (m)
ε_o	open porosity (–)
ε	thermal emittance (–)
$\Phi(e_i,e_j)$	scattering function between incoming (direction vector e_i) and outgoing ray (direction vector e_j) (–)
Ψ	empirical parameter (–)
σ	Stefan-Boltzmann constant ($W/(m^2 K^4)$)
ρ_i	density of fluid within control volume i (kg/m^3)
μ_f	dynamic viscosity of fluid (kg/(m s))
μ_i	polar angle cosine for discretized ray direction with index i in Discrete Ordinate Model (–) weighting factor for discretized ray direction with index i in Discrete Ordinate Model (–)
κ_α	absorption coefficient (m^{-1})
κ_s	scattering coefficient (m^{-1})

photovoltaic power), solar thermal power plants can provide dispatchable power by means of thermal energy storage and/or hybridization with renewable or conventional fuels. Given the abundant amount of solar power available for terrestrial solar collectors (85 PW) [1], which exceeds the current world's power demand (15 TW) several thousand times [1], CSP is a highly promising alternative to conventional fossil-fuel or nuclear technology, setting new standards in terms of environmental impact, sustainability, safety, and thus quality of life.

The majority of today's CSP plants are based on the parabolic trough collector technology that has been established on commercial level since the 1980s (SEGS plants in California, USA [2]). Back then, annual solar-to-electric conversion efficiencies achieved values up to 10.6% [2] and are nowadays still not higher than 14–15% [3]. Achieved peak solar-to-electric conversion efficiencies are in the range of 20–25% [4]. Fundamentally, this efficiency constraint is due to the limited operating temperature ($\approx$400 °C) of the applied heat transfer fluid (thermal oil) [5].

Clearly, the move to other heat transfer fluids that enable higher operating temperatures is a must. Viable options are for example molten salts (upper limit at about 600 °C [6]) and air. Another option is the direct heating of the power cycle's working fluid in the solar receiver (e.g. direct steam generation). However, also a solar collector/receiver technology change is inevitable, since higher receiver operating temperatures are only feasible with high area concentration ratios [7]. Instead of the conventional parabolic trough technology (line focusing), the power tower concept (point focusing) is, in this context, much more favorable.

The solar receiver or solar absorber is a key component of a CSP plant and must be optimized to keep thermal losses as low as possible, in order to maximize its thermal efficiency. This work will focus on volumetric absorbers (see Ref. [8] for a detailed review of volumetric receivers) for central receiver or power tower plants. In particular, it will focus on the optimization of ceramic foam absorbers working with air as heat transfer fluid at atmospheric pressure.

In the following, a detailed literature review will be given on the topic of ceramic foam absorbers, as well as on the application of multi-layer absorber configurations with gradual property variations in direction of air flow, a likely enhancement method of the absorber's thermal performance.

Ceramic foam was already proposed as promising solar absorber material in the early 1990s by Chavez & Chaza [9] (alumina foam) and later on again by Fend et al. [10,11] (silicon carbide foam). However, although ceramic foam material has advantages regarding heat transfer, solar flux penetration, as well as radial heat transport, this volumetric absorber technology has not been applied in recent non-pressurized solar receiver demonstration projects, where ceramic honeycombs were

chosen instead [8,12–14]. Nevertheless, ceramic SiC foam with a cell density of 20 PPI was applied in the SOLGATE [15] project for the pressurized high-temperature volumetric absorber behind the quartz window.

With the objective to investigate absorber materials other than metallic wire meshes (at that time being evaluated by the PHOEBUS consortium [16]) Chavez & Chaza [9] designed, fabricated and tested a porous ceramic alumina foam material as volumetric solar absorber. The absorber mean efficiency was in the order of 65% at 550 °C air outlet temperature. At the peak outlet temperature of 730 °C, the efficiency went down to just 54%, which gave reason for further absorber optimization. Nevertheless, they successfully demonstrated the suitability of ceramic foam as absorber material as it withstood rapid changes in flux levels and peak fluxes as high as 824 kW/m^2. No cracking or degradation was observed after over 70 h of testing.

Pitz-Paal et al. [17] published an important work on solar absorber performance and flow stability. They analyzed the influence of a three-dimensional irradiance distribution on fluid flow and radial heat transfer. Their model helped to explain how thermal efficiencies and temperature distributions are strongly influenced by non-homogenous irradiance profiles. Among a variety of volumetric absorber samples, they also experimentally investigated ceramic SiC foam with a porosity of 78.2% and a cell density of 30 pores per inch (PPI). Obtained thermal efficiency values of this SiC foam were around 60% at 800 °C and around 64% at 700 °C.

Later, Fend et al. [10] again considered ceramic foam as absorber material. They applied sintered silicon carbide (SSiC) supplied by the Fraunhofer-IKTS. For the first time, they proposed a combination of two different cell densities in a stacked absorber configuration in direction of air flow. The front part of the absorber had a cell density of 80 PPI and the rear part had a cell density of 20 PPI. The motivation for this stacked configuration was to have a high cell density in the extinction zone only, and to reduce cell density in the rear part in order to reduce flow resistance and increase effective heat conductivity.

Bai [18] developed a 1-D numerical model (in direction of air flow) of a ceramic foam absorber, assuming uniform incident radiative flux, negligible radial heat conduction, negligible radiative losses at the front surface, as well as a perfectly insulated absorber at its radial boundaries (adiabatic conditions). Furthermore, the air was considered as ideal gas. An important conclusion was that air flow resistance rises with increasing air outlet temperatures, which is fundamentally due to the fact that the air viscosity increases with higher temperatures. Consequently, having a non-uniform solar flux distribution at the absorber entrance plane, hotter parts will have higher flow resistance leading to increased air flow in colder regions, leaving hotter zones even less cooled – the self-amplifying hot-spot effect.

Wu et al. [19] developed a generalized macroscopic CFD model of a ceramic foam solar absorber. Instead of resolving the flow down to pore scale of the foam, they used a volume averaging technique. This approach greatly reduced complexity of the physical problem. The following assumptions were made: uniform porosity; steady and turbulent flow field; constant thermo-physical properties of the solid; negligible effects of buoyancy, negligible hydrodynamic dispersion, negligible viscous dissipation and negligible thermal expansion; local thermal non-equilibrium (LTNE) between solid and fluid domain. Radiative transfer was considered applying the lowest-order case of the method of spherical harmonics [20], the so-called P_1-approximation. The foam was considered as absorbing, emitting and isotropic scattering medium with homogenous and gray radiative properties. Wu et al. [19] concluded that in terms of thermal efficiency, a cell size of 1–2 mm combined with the highest possible level of porosity presents the most favorable choice for the solar absorber structure.

Wu & Wang [21] focused on a transient model of ceramic foam absorber material using the CFD software Fluent. Similar to Ref. [19], local thermal non-equilibrium is assumed and the radiative transfer is solved applying the P_1-approximation. With the model, they showed the transient response of the absorber under sudden heat flux variations.

Kribus et al. [22] presented a 1-D model of a ceramic foam absorber giving emphasis on the implementation of the radiative heat transport, leading to a model that considers the most significant physical processes and that is simple enough for extensive parametric studies. As previous works, they considered local thermal non-equilibrium, i.e. the solid and fluid phases have separate temperature distributions as function of absorber depth (the modeled dimension). The radiative heat transport was implemented with 4 different methods: (i) the so-called two-flux approximation (also referred to as Schuster-Schwarzschild approximation [20] named after its two independent authors), (ii) the 4th order discrete ordinate method (commonly known as S_4-approximation [20]), (iii) the already above mentioned P_1-approximation, and (iv) the Monte Carlo method for thermal radiation [20]. After a comparison of the four different methods, the S_4-approximation was finally chosen for the parametric study due to its high accuracy and very fast computation. The parametric study again confirmed the strong dependence of the absorber's efficiency on the porosity, i.e. the higher the porosity, the higher is the efficiency. However, unlike stated in Ref. [19], it was found that higher pore size leads to higher efficiencies. The best case (thermal efficiency around 0.76) had 4 mm of cell diameter and a porosity of 0.9, which represents the upper practical porosity limit with current manufacturing techniques. The impact of both parameters is to shift the solar absorption process further inside the absorbing structure, allowing a gradual temperature increase from the front towards the back. Further efficiency improvement could only be achieved with hypothetically enhanced convective heat transfer and spectral selectivity. The possibility of graded properties (varying over the absorber depth) was not considered.

Mey-Cloutier et al. [23] presented detailed experimental work on several ceramic foam samples (silicon carbide SiC, alumina Al_2O_3, and zirconia ZrO_2) covering a range of porosity (72–92%) and cell density (5–20 PPI). The purpose of the experimental campaigns was to quantify the performances of different ceramic foams as volumetric solar absorbers. Two trends were observed regarding cell density: (i) on the one hand, higher efficiency was observed with lower cell density, due to deeper penetration of solar irradiation into the structure; (ii) on the other hand, higher efficiency was observed with higher cell density because of improved convective heat transfer. Concerning the sample porosity, it was observed that the best efficiency was obtained from a SiC sample with the lowest porosity (72%). It has to be emphasized that the number of samples tested was quite low (11 pieces in total) and that the influence of the different material properties may have falsified the conclusions about the effects of cell density and porosity. Additionally, there is measurement uncertainty related to the experimental results, which makes a final conclusion very difficult.

Li et al. [24] discussed a transient 1-D system level model of an open-loop air receiver plant with thermal energy storage. Ceramic foam (SiC) was used as absorber material. The absorber model was implemented with the following assumptions: uniform solar irradiance and mass flow distribution across absorber aperture; isotropic foam; physical properties of the foam are independent of temperature. The solar heat input was assumed as inverse exponential fixed heat source without modeling radiative transport in detail. The model was successfully validated against experimental data. Future work of the authors will focus on optimization of thermal performance and plant operating strategies.

Regarding the gradual-porosity or multi-layer volumetric absorber configurations, the following summary can be given: It is an innovation that addresses the main thermal problems of the technology. The basic objectives of gradual porosity are to allow a deeper solar flux penetration, so that the maximum temperature is achieved inside of the absorber, and to reduce the frontal surface temperature of the absorber which reduces the frontal thermal losses. The main contributions to the gradual-porosity or multi-layer configurations are briefly summarized.

Hellmuth et al. [25–27] proposed for the first time a multi-layered absorber with wire meshes at the experimental level. Firstly, they tested the Bechtel 1 absorber at lab scale with 17 circular screens of 67 mm diameter. The first nine screens had one layer each of 0.11 mm diameter wire mesh, and the remaining eight screens had four layers each of 0.21 mm diameter wire mesh with a 3.2 mm separation between them. After reasonable results in lab-scale tests (efficiency ranged from 80% to 69% at outlet air temperatures of 320 °C to 820 °C) they scaled up to a 250 kW prototype with a similar multi-layered concept. The latter absorber thermal efficiencies ranged from 90% at 200 °C to 66% at 563 °C, in contrast to the expected thermal efficiency of 90% at 700 °C.

Avila-Marin et al. [28] took up again the gradual porosity concept at the experimental level with dense wire mesh stack in contrast to the sparse stack of Hellmuth. On the contrary to previous works with wire meshes, this work presented a higher wire diameter in the first layers to assure a good mechanical performance, showing a good thermal and mechanical behavior.

Avila-Marin [29] analyzed the optical and geometrical parameters of the single and multi-layer concept with metallic wire mesh at the experimental and numerical level. It was presented that the performance of the absorber is maximized when the first layer has as high porosity and low extinction coefficient as possible, together with a second layer with the highest specific surface area possible.

Roldan et al. [30] published an important work where the thermal evaluation of different absorber configurations was performed with a 2-D numerical model in Fluent. This paper analyzed single-porosity against gradual (increasing and decreasing) porosity configurations. The work presents some assumptions in order to reduce the computational costs: local thermal equilibrium (LTE), steady-state conditions, negligible effect of gravity and air properties correlations. They concluded, as an initial prediction of the behavior of the gradual-porosity concept, that the decreasing-porosity configuration according to depth has the best thermal performance among the different configurations analyzed.

Chen et al. [31] developed a 2-D numerical model in Fluent where a double-layer configuration was studied for a ceramic foam. This model presented the following assumptions: LTNE coupled with the P1 model for solving the radiative transfer equation, steady and incompressible air flow, constant ceramic properties in each layer, the foam was considered as a gray, optically thick, absorbing, emitting and isotropic scattering medium, and the walls of the receiver were adiabatic. They concluded that the thickness of the first porous layer has significant effect on the temperature field and pressure drop. Compared with the increasing-porosity configuration, the decreasing-porosity configuration tends to achieve higher air outlet temperature and lower solid inlet temperature. Moreover, the increasing design of mean cell size shows improved performance compared to the decreasing design.

In summary, much work has already been spent on the topic of ceramic foam and multi-layer absorbers, but it is not yet clear which properties and foam combinations, in the case of gradual property variations, lead to the optimum solar absorber performance. It is the aim of this work to further analyze the topic with numerical and experimental methods in order to give well justified design recommendations for the development of ceramic foam solar absorbers. In particular, two different 1-D model types with local thermal non-equilibrium (LTNE) have been developed independently at CENER and Fraunhofer-IKTS. The modeling of radiation propagation inside the foam is considered via two approaches. One approach is based on a discrete-ordinate solution of the radiation transport equation; the other imposes the solar flux defining an exponential attenuation, as derived from Bouguer's law, and considering thermal radiation transport according to Rosseland's diffusion approximation. Both models have been successfully checked for consistency against experimental data (for single and multi-layer configurations) obtained at a 4 kW solar simulator. Also, key simulation results of both models have been compared, showing good agreement. Then, both numerical models have been used for an extensive parametric optimization of single and multi-layer configurations for highest thermal efficiency, which has not been accomplished so far in the literature.

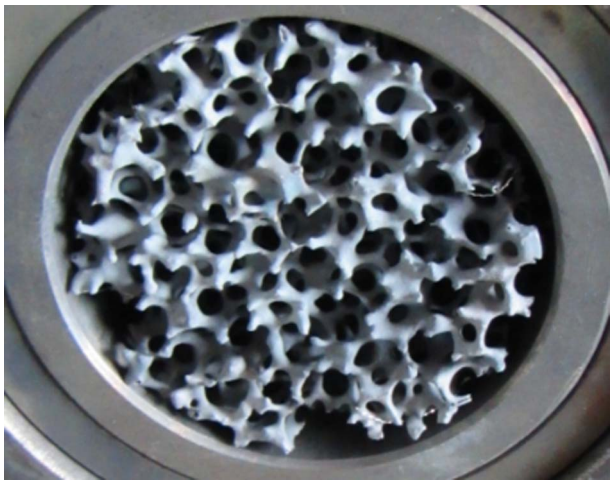

Fig. 1. Ceramic foam absorber sample placed in solar simulator test bed.

This work is structured as follows: Section 2 gives a short introduction to ceramic foams and their characterization. Section 3 presents the numerical models and the comparison of simulation results. Section 4 compares simulation results with experimental data. Section 5 includes parametric simulation runs and foam parameter optimization. Section 6 concludes.

2. Ceramic foam characterization

Ceramic foam (see Fig. 1) is a positive image of a polymer foam of chosen pore density [32,33]. During the first production process, the polymer foam, which is usually polyurethane, is submersed in ceramic slurry. Then, excess slurry is removed from the wetted foam via squeezing and kneading. Next, the wet foam is dried, and then heated to high temperatures, where the polymer base vaporizes or burns and the ceramic sinters [32,33]. Characteristic for the so-called replication technique is a remaining internal void volume in the ceramic foam struts where the polymer foam was originally placed.

Thus, due to this process, the final shape of the ceramic foam is intrinsically dependent on both the geometry of the polymer foam and the coating thickness of the ceramic slurry. Thus, it makes sense to use already existing characterization standards for polymer foam, since this defines the base geometry. Nevertheless, due to different shrinkage behavior of the ceramics applied, the final cell density of the ceramic foam may differ significantly from its polymer foam base.

Polymer foams are typically characterized via the parameter cell or pore density according to the norm ASTM D 3576-77, which is based on a mean value of number of cells on a specified linear distance. The unit is thus pores per inch (PPI) [33]. The higher the number is, the more pores or cells exist, i.e. the smaller are the cells. The lower the number is, the fewer pores or cells exist, i.e. the larger are the cells. Polyurethane foam is commercially available between 8 and 90 PPI [33]. The inverse value of the pore density corresponds to a mean cell size (in inch), which however does not differentiate between real cell diameter and window diameter. This differentiation between cell diameter and window diameter is a result of the typical foam geometry that is governed by the natural arrangement of gas bubbles during the foaming process. Thus, wherever neighboring gas bubbles touch each other, a window forms (window diameter), whereas for the case of the gas bubble itself, a cell forms (cell diameter). As a good rule of thumb, the diameter of the windows d_w is approximately one third of the cell diameter d_c [33]:

$$d_w \approx \frac{d_c}{3} \tag{1}$$

The open porosity ε_o may be determined as follows [34] for circular strut cross sections (assuming idealized tetrakaidecahedron geometry):

$$\varepsilon_o = 1 - \frac{9.425}{8\cdot\sqrt{2}}\cdot\left(\frac{t_s}{l}\right)^2 + \frac{3.33}{8\cdot\sqrt{2}}\cdot\left(\frac{t_s}{l}\right)^3 \tag{2}$$

The specific surface area S_v may be calculated as follows (circular strut cross sections) [35]:

$$S_v = 4.867\cdot\frac{[1-0.971\cdot(1-\varepsilon_o)^{0.5}]}{d_w\cdot(1-\varepsilon_o)^{0.5}}\cdot(1-\varepsilon_o) \tag{3}$$

3. The numerical modeling

The behavior of volumetric solar receivers is a quite complex phenomenon, governed by scattering/absorption processes of the incident solar flux, thermal radiation, convection and conduction. Thus, the modeling of such a receiver is a rather cumbersome task, which makes certain modeling assumptions crucial in order to simplify the problem. Common assumptions are that the ceramic foam (the porous absorber material) has constant and homogenous properties, features isotropic scattering, and behaves as gray emitting and absorbing body [19,31].

In principal, one can differentiate between two types of models. On the one hand several studies apply porous media CFD models (e.g. [19,21,36]), while other authors estimate the absorber's behavior applying an one-dimensional approach [17,22], only taking into account changes in axial direction normal to the absorber's front face, where the absorber model comprises two phases, solid (porous absorber) and fluid (air). The latter approach leads to a relatively simple model setup, having two different temperature distributions along the absorber's depth, one for the fluid (T_{air}) and one for the solid ($T_{absorber}$), i.e. local thermal non-equilibrium (LTNE) [22].

Regarding the CFD approach, in principal, two modeling options exist. On the one hand it is possible to model the foam's geometry in detail (e.g. assuming many aligned idealized tetrakaidecahedron cells) and to simulate a representative section of the absorber by resolving flow field, temperature field as well as the radiation scattering and absorption process. On the other hand, it is possible to introduce a so-called equivalent homogenous model (EHM), also known as the porous medium approach.

In this work, two 1-D model types with local thermal non-equilibrium (LTNE) are used, differing in the modeling of radiation propagation inside the foam. One approach is based on a discrete-ordinate solution of the radiation transport equation; the other imposes the solar flux defining an exponential attenuation [37], as derived from Bouguer's law [38], and considering thermal radiation transport according

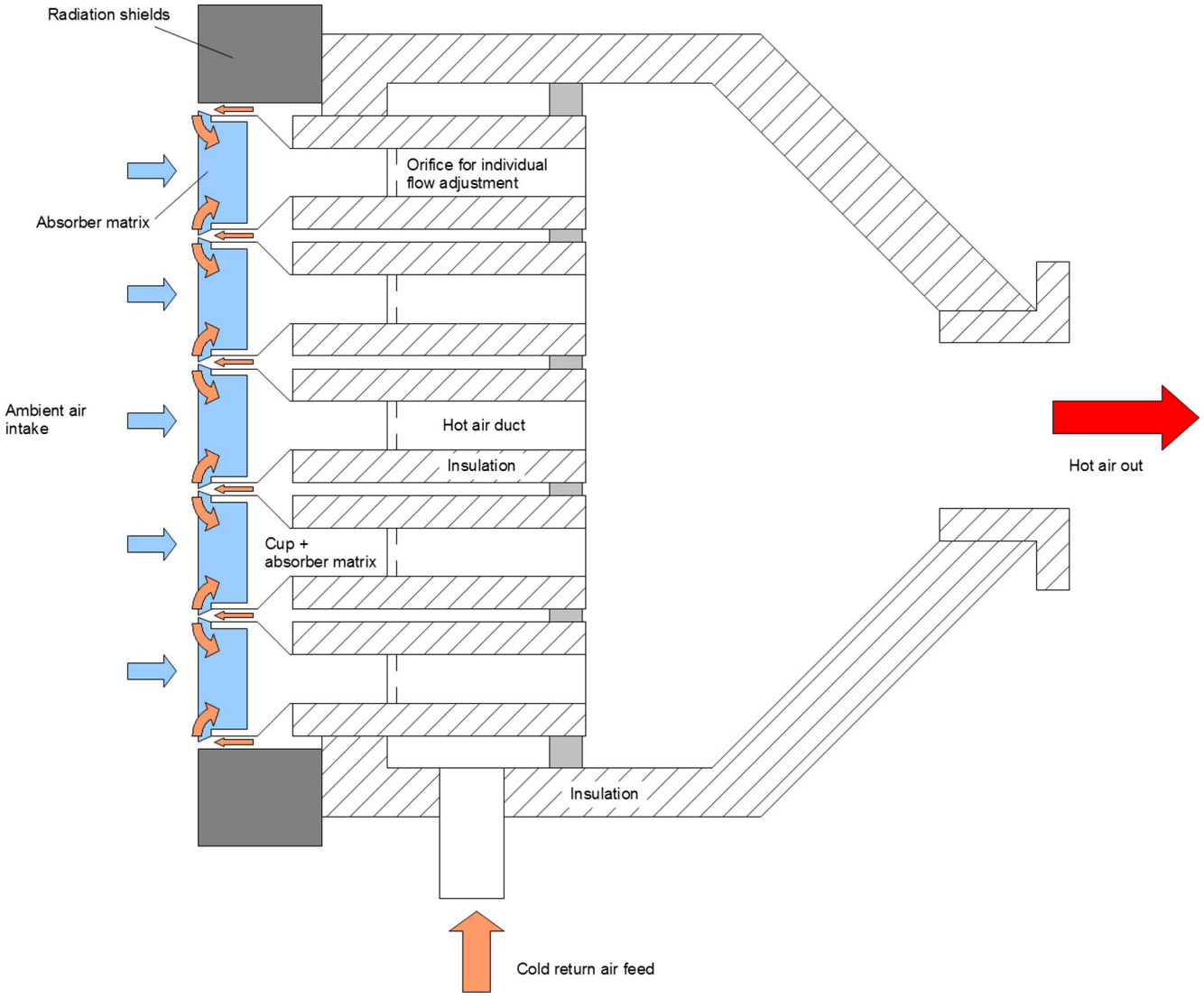

Fig. 2. Volumetric solar receiver scheme.

to Rosseland's diffusion approximation [20,38]. The motivation for the 1-D modeling approach lies in the short simulation time, enabling extensive parametric optimization runs.

3.1. Assumptions for the 1-D modeling of the absorber

A volumetric air solar receiver unit is typically composed of an array of cups, where each cup contains the solar absorber matrix (see Fig. 2) [13]. The total number of cups depends on the necessary thermal power for the specific plant. This modular receiver concept is required to individually adjust the air flow on cup level, in order to take variations of incident solar flux into account, being able to reach similar outlet temperatures for each cup. Although it is task of the aiming strategy of the heliostat field to achieve a homogenous solar flux map, it is difficult to achieve this in practice, e.g. due to heliostat calibration issues, facet shape errors and given heliostat focal spot sizes. Thus, the solar flux map on the receiver is typically not homogenous and the solar absorber has to be modular to adjust air flow and outlet temperature for each module individually.

When looking at a single cup however, the incident solar flux may be considered as homogenous for the relatively small absorber area (140 × 140 mm), which makes it possible to model the solar absorber matrix only in one dimension, the direction normal to the absorber front face (see Fig. 3). Fig. 3 gives an overview of one single cup, also indicating the modeling dimension, and a detailed view of the absorber's ceramic foam structure.

According to the local thermal non-equilibrium approach, the domain will be discretized normal to the absorber front face, introducing separate temperature nodes/volumes for the solid phase and for the fluid phase, respectively. The fluid phase is modeled according to the finite volume method. The solid phase is modeled according to a distributed lumped capacitance approach. In the following, each model component will be explained, indicating also the differences of the two applied modeling approaches.

3.2. Solar irradiance absorption, scattering process and thermal transport in the foam

The key phenomenon in a solar absorber is radiation transport. Thus, the most detailed modeling approach is the numerical solution of the radiation transport equation (RTE). In this work, this is done according to the discrete-ordinate (DO) method, implemented at Fraunhofer-IKTS (in the following referred to as detailed DO radiation model). It takes into account the semi-transparent thermal radiation transfer characteristics of the foam. The model is based on a homogenized approach and includes volumetric thermal radiation transport and interactions (absorption, scattering) within the foam, additional to thermal transport in the solid and the fluid phase (LTNE approach) and mass transport. The model intrinsically provides locally graded absorption and emission characteristics over a distributed subsurface zone and net transport of non-equilibrium radiative energy inside the foam domain.

The Discrete Ordinate (DO) method uses a directional discretization of the Radiation Transfer Equation (RTE) for radiative intensity over a reduced set of discrete beam directions (Discrete Ordinates, S8 approach: 80 directions). In the 1-D approach for problems with cylindrical symmetry along a main axis (here: position s perpendicular to absorber surface, parallel to solar incident radiation) a further reduction is possible by subsuming beams with the same polar angle cosine μ_j into one group indexed by j with a weighting factor ω_j:

$$\pm \frac{\mu_j}{\mathrm{K}} \frac{\partial I_j^{\pm}}{\partial s} = \frac{\kappa_a}{\beta} \cdot n^2 \cdot \frac{\sigma \cdot T^4}{\pi} - I_j^{\pm} + \frac{\kappa_s}{\mathrm{K}} \frac{1}{4\pi} \cdot \sum_j \varpi_j \cdot I_j^{\pm} \cdot \Phi(e_i, e_j) \tag{4}$$

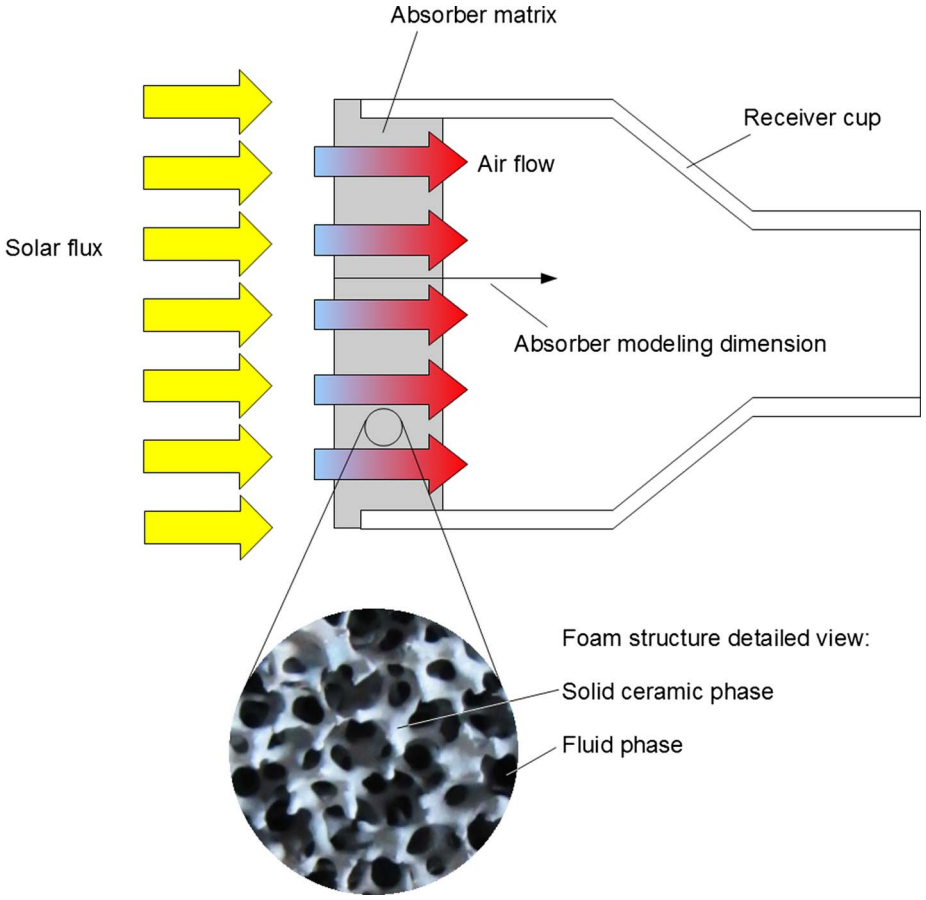

Fig. 3. Receiver cup scheme and foam structure detailed view.

$I_j^{\pm}$ represents the intensity of the Discrete Ordinate group j, distinguishing between a positive (+) or negative (−) direction of propagation and $\Phi(e_i,e_j)$ the scattering function (e_i and e_j, normal vector of incoming and scattered beam direction), which was assumed as 1 (isotropic scattering) for the present model. A coupling between thermal and radiative balance equations is provided with the volumetric heat source term $\dot{Q}_{rad,V}$

$$\dot{Q}_{rad,V} = -\frac{\partial q}{\partial s} \tag{5}$$

and $\frac{\partial q}{\partial s}$ as gradient of net radiative flow q with radiation path length s

$$q = \int_{4\pi} I(\mathbf{s})\cdot\mathbf{s}\cdot d\Omega = \sum_{k}^{N/2} \varpi_k'\cdot\mu_k\cdot(I_k^{+}-I_k^{-}), \tag{6}$$

while the local temperature T appears in the black body emission term of the RTE.

The DO method is described elsewhere (see Modest [20]) in more detail. In the homogenized one phase approach, the foam is characterized as a semitransparent continuum material with effective volumetric extinction K, absorption κ_α and scattering κ_s coefficients, applying common correlations (Hendricks and Howell [39]), with ε characterizing the emissivity of the bulk structural material:

$$\kappa_\alpha = \varepsilon\cdot\beta_V \quad \text{and} \quad \kappa_s = (1-\varepsilon)\cdot\beta_V \tag{7}$$

A simplified approach to the above is to impose the solar flux defining an exponential attenuation [37], as derived from Bouguer's law [38], and considering thermal radiation transport according to Rosseland's diffusion approximation [20,38]. According to Bouguer's law [38], the intensity of mono-chromatic radiation along a path is attenuated exponentially while passing through an absorbing-scattering medium. The exponent is equal to the integral of the local extinction coefficient over the path length traversed by the radiation [38]. The extinction coefficient K is a physical property of the material, having the unit of reciprocal length [38]. When assumed constant along the path of radiation, the extinction coefficient can be interpreted as the reciprocal of the radiation mean penetration distance [38].

According to Siegel and Howell [38], the radiation intensity i as function of medium depth z, i.e. $i(z)$, can be described as follows:

$$i(z) = i_{(z=0)}\cdot e^{-K\cdot z} \tag{8}$$

when assuming the extinction coefficient K independent of medium depth. The radiation intensity i has the unit of radiation energy propagating per unit time, per unit of projected area and per unit solid angle [38].

Applying this exponential attenuation concept to the solar flux penetration within the ceramic foam absorber, the impinging solar irradiance (coming from the concentration optics) is going to be distributed according to an exponential attenuation function within the absorbing medium.

When implementing the above in the 1-D numerical simulation code where a certain spatial discretization is applied, a straightforward approach is to define the fraction of incident power per spatial node simply as the ratio of areas under the inverse exponential curve ($e^{-K\cdot z}$). In particular, the ratio of the area under the inverse exponential function at the specific discrete location (node grid section) A_i to the total area A_0 under the curve, that is, when z approaches infinity. Fig. 4 displays the concept. At node number two of the 1-D discretization the area ratio would be (see Fig. 4):

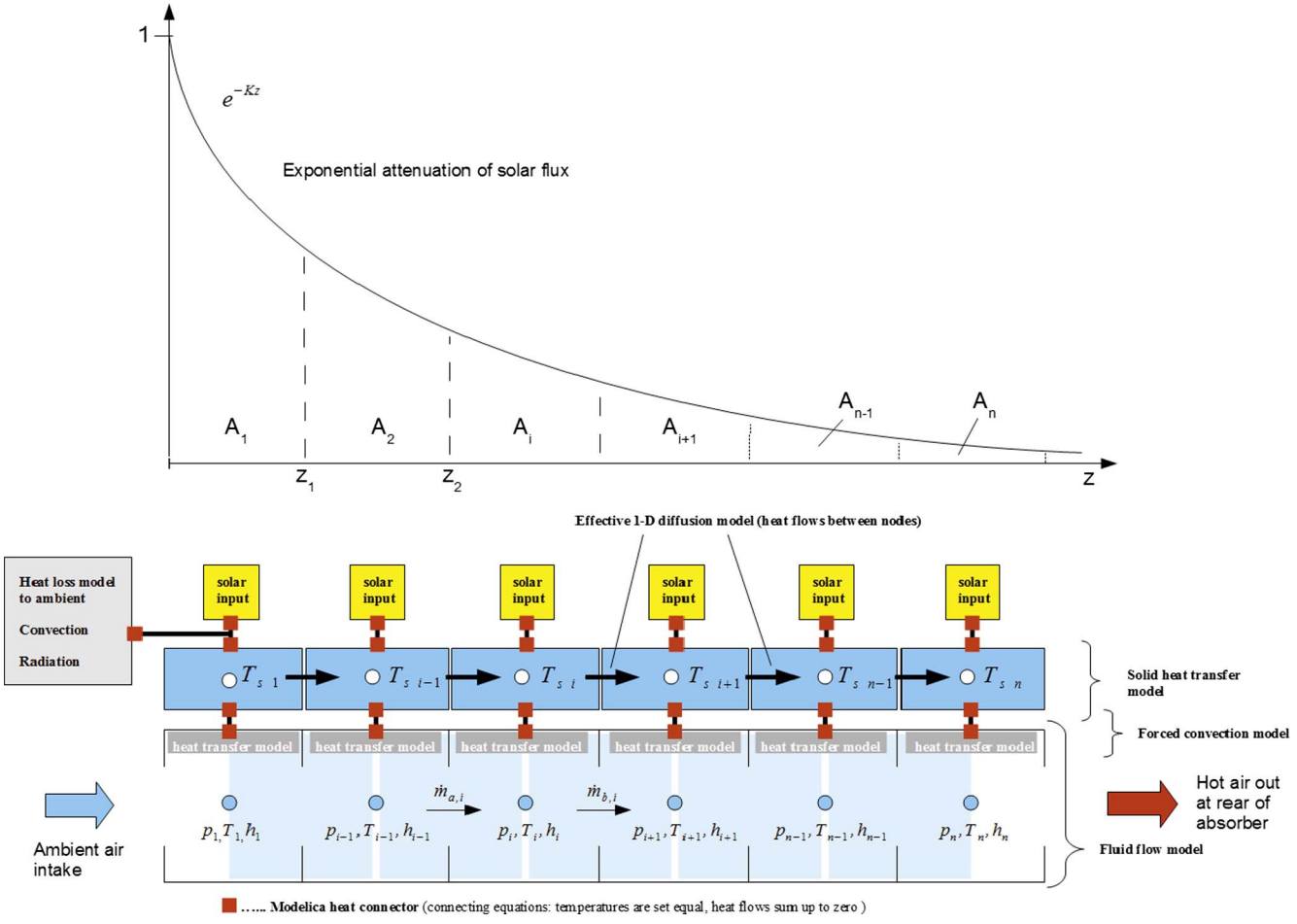

Fig. 4. One-dimensional volumetric absorber model scheme in Modelica (simplified radiation model – CENER).

$$R_2 = \frac{A_2}{A_0} = \frac{1/K\cdot(e^{-Kz_1} - e^{-Kz_2})}{1/K\cdot(1 - e^{-K\infty})} = \frac{e^{-Kz_1} - e^{-Kz_2}}{1} = e^{-Kz_1} - e^{-Kz_2} \quad (9)$$

According to the above, the solar flux I_2 incident at node number 2 can be described as follows:

$$I_2 = I_0 \cdot R_2 \quad (10)$$

where I_0 is the solar flux (in W/m^2) incident at the absorber's front face, coming from the concentration optics, i.e. the heliostat field.

Generally, it can be written:

$$I_i = I_0 \cdot R_i \quad (11)$$

To obtain the heat flow values that are absorbed at each node i ("solar input" on Fig. 4), the incident solar flux I_i at each node needs to be multiplied by the solar absorptance of the foam material and the absorber aperture area. The solar absorptance has been set to 0.9 for the simulations presented. This value has been obtained from a measurement campaign of several foam samples supplied by Fraunhofer IKTS.

Finally, the extinction coefficient K must be determined experimentally for a specific foam material. According to Hendricks and Howell [39], the extinction coefficient may be related to porosity and pore diameter as follows:

$$K = \frac{\Psi\cdot(1-\varepsilon_o)}{d_c} \quad (12)$$

where Ψ is an empirical parameter, giving good results for OB SiC with the value of 4.8 [39].

Next, for both model types, thermal conduction inside the foam must be modeled.

The conductive contribution of the foam material can be estimated as given in Eq. (13). This correlation is based on the work of Schuetz & Glicksman [40] and has been successfully applied by Wu et al. [19,21] as well as Xia et al. [41].

$$k_{con} = \frac{1-\varepsilon_o}{3}\cdot k_s \quad (13)$$

The pure phase thermal conductivity k_s is calculated according to Endisch [42] for SSiC foam (supplied by Fraunhofer IKTS).

Endisch [42] provides the following empirical correlation for SSiC (T = temperature in K):

$$k_s = 24.84917 + 98.5\cdot e^{\left(\frac{-T-22.69}{363.587}\right)} \quad (14)$$

Due to the complex macroscopic and microscopic structure, the determination of the solid conductivity k_s of SSiC foam material is not trivial. Whilst conventional SiC solid structures provide 125 W/(m K) at room temperature and about 40 W/(m K) at 1000 °C [43], the thermal conductivity of the solid network structure (struts) of SiC foam depends furthermore on impurities due to the fabrication process and is typically lower. Fig. 5 shows the solid structure conductivity of SSiC according to Eq. (14).

For the simplified imposed radiation model, the radiative heat transfer within the foam needs to be considered additionally.

In the literature, the consideration of the radiative heat transfer ranges from simplest approaches, only taking into account an increased effective thermal conductivity [44] (according to Rosseland's diffusion approximation [20,38]), to relatively complex and computationally demanding implementations such as Monte Carlo techniques [20,22].

Here, the simplest approach is taken, considering thermal radiation via an effective thermal conductivity, which is typically applied in the modeling of fixed-bed combustion processes (e.g. fixed-bed biomass combustion [45,46] or coal fires [47]). This approach assumes a porous optically thick medium, where the internal radiative heat transport can be described as a diffusive process [38,48,49]. In an optically thick or dense medium, the radiation can only travel a short distance before being absorbed. If furthermore this radiation penetration distance is small compared to the distance over which significant temperature changes occur, it can be shown that it is possible to transform the integral-type equations that result from the radiative energy balance into a diffusion equation [38], having the form of a conduction equation. Of course, for the case of a solar absorber, the application of such a simplified radiation model needs to be discussed, since the radiation penetration distance and the distance over which significant temperature changes occur may be in the same order of magnitude. For instance, having a radiation penetration distance of about 1–4 mm (≈cell size of the foam), then we have, according to the later on presented simulation results, up to about 140 °C of temperature gradient over ≈5 mm of foam depth. Thus, when applying this simplified radiation model in the code, the simulation results need to be checked against experimental data in order to justify its suitability.

The effective thermal conductivity is typically composed of a conductive and a radiative contribution [46,50]:

$$k_{eff} = k_{con} + k_{rad} \quad (15)$$

The radiative contribution is estimated according to Dietrich et al. [51]:

$$k_{rad} = \frac{16\cdot\sigma\cdot T^3}{3\cdot[1.3\cdot d_w^{-1}\cdot(1-\varepsilon_o)^{1/3}]} \quad (16)$$

The above correlations (Eqs. (15) and (16)) are used in this work for estimating the effective thermal conductivity for the effective 1-D diffusion model (see Fig. 4).

It is important to note that the fluid, the air, is assumed as non-participating medium for radiative heat transfer. Since elementary gases as nitrogen and oxygen and elementary gas mixtures (dry air) have a symmetrical molecular structure, and neither emit, nor absorb radiation in the temperature ranges under consideration [52], the heat transfer via radiation can only be considered between the surfaces of the foam structure.

3.3. The modeling of the 1-D fluid flow

The air flow across the absorber is modeled using the finite volume method (FVM), defining the mass and energy balances in terms of net mass flow, net enthalpy flow, and net heat flow $\dot{Q}_{net}$, for each control volume i (see Fig. 6). This can be written as follows:

$$m_i = V_i\cdot\rho_i \quad (17)$$

$$\frac{dm_i}{dt} = \dot{m}_{a,i} - \dot{m}_{b,i} \quad (18)$$

$$U_i = m_i\cdot u_i \quad (19)$$

$$\frac{dU_i}{dt} = \dot{m}_{a,i}\cdot h_{a,i} - \dot{m}_{b,i}\cdot h_{b,i} + \dot{Q}_{net,i} \quad (20)$$

The air is modeled as ideal gas, calculating specific enthalpy and internal energy according to McBride et al. [54]. They provided polynomial based specific heat capacity data for a great variety of gases and

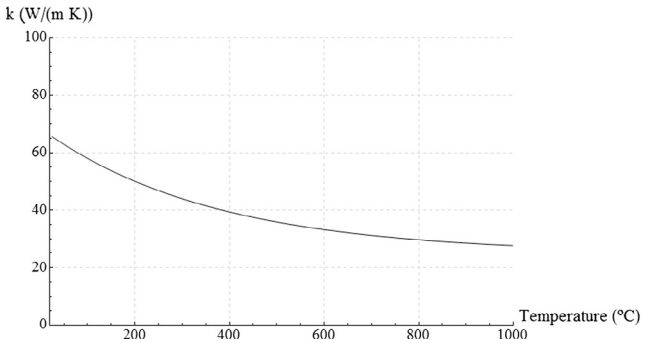

Fig. 5. SSiC foam solid thermal conductivity (k_s) as function of temperature according to Eq. (14).

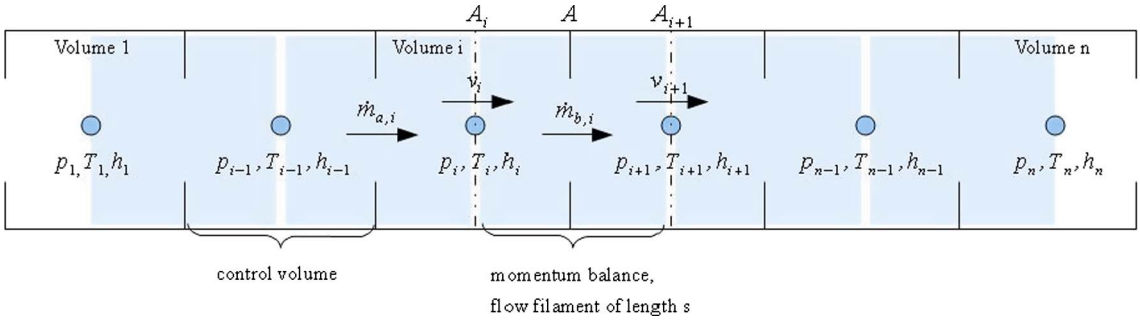

Fig. 6. Finite volume discretization scheme according to the staggered grid approach [53]

for wide temperature ranges. Thus, by simply replacing the coefficients of the polynomials, the same code can be reused for many different kinds of gases. However, the transport properties, thermal conductivity and dynamic viscosity, had to be implemented additionally. This has been done according to Kadoya et al. [55]. They provided function-based viscosity and thermal conductivity data for dry air in the gaseous phase for temperatures from 85 to 2000 K, and pressures up to 100 MPa.

As a next step, since a local thermal non-equilibrium (LTNE) model is applied, it is necessary to determine the convective heat transfer coefficient (interstitial heat transfer coefficient) between the solid and the fluid, fulfilling Newton's convective heat transfer law (see Fig. 4 – "heat transfer model"):

$$\dot{Q}_{neti} = h_{fi} \cdot A_{surface} \cdot (T_{si} - T_i) \tag{21}$$

The convective heat transfer coefficient between solid structure and air flow is a fundamental parameter of the model and has to be estimated by an experimentally confirmed Nusselt number correlation. Dietrich [56] provided the following correlation based on experimental data:

$$Nu = \frac{h_f \cdot d_h}{k_f} = 0.31 \cdot Hg^{1/3} \cdot Pr^{1/3} \tag{22}$$

where the Hagen number (Hg) is defined as follows:

$$Hg = \frac{\Delta p}{\Delta L} \cdot \frac{\rho_f \cdot d_h^3}{\mu_f^2} \tag{23}$$

and, where the pressure drop (Δp) per depth of foam (ΔL) is given as follows [57]:

$$\frac{\Delta p}{\Delta L} = 110 \cdot \frac{\mu_f}{\varepsilon_o \cdot d_h^2} \cdot v_s + 1.45 \cdot \frac{\rho_f}{\varepsilon_o^2 \cdot d_h} \cdot v_s^2 \tag{24}$$

It is important to note that the hydraulic diameter (d_h) is taken as characteristic length, which is defined as follows [57]:

$$d_h = \frac{4 \cdot \varepsilon_o}{2.87/(t_s + d_w) \cdot (1 - \varepsilon_o)^{0.25}} \tag{25}$$

This heat transfer correlation (Eq. (22)) has recently been successfully benchmarked by Xia et al. [41] against other correlations in the literature and is expected to also provide good results in the present work.

Also note that the applied Nusselt number correlation (Eq. (22)) [41] is based on the superficial flow velocity, which is also known as "empty tube" velocity [58], disregarding the presence of the solid phase, the foam material. The superficial flow velocity v_s is thus simply obtained by Eq. (26):

$$v_s = \frac{\dot{m}}{\rho_f \cdot A} \tag{26}$$

However, the true velocity within the porous matrix will be greater, as the fluid has to squeeze through the smaller available area. An approximation of the true velocity is the so-called interstitial velocity v, which is obtained by dividing the superficial flow velocity by the porosity [58]:

$$v = \frac{v_s}{\varepsilon_o} \tag{27}$$

Note that the interstitial heat transfer coefficient h_f is related to the volumetric heat transfer coefficient h_v according to the following equation [41]:

$$h_v = h_f \cdot S_v \tag{28}$$

Finally, the last correlation necessary for completing the 1-D fluid flow model is the pressure drop correlation, which relates mass flow and pressure difference between fluid control volumes. Here, Eq. (24) is used.

3.4. Model boundary conditions

Finally, the boundary conditions at the irradiated side of the absorber (air entry) and at the non-irradiated side (air exit) have to be defined.

For the detailed DO radiation model, the incident solar radiation intensity is introduced as a Dirichlet boundary condition to the RTE intensity balance at the inlet side. The DO model allows considering the focused characteristics of the incident solar radiation: in the simplest possible case assigning intensity values to a single selected ordinate group (beam direction) only (group j = 4 with minimum tilt angle cosine $\mu_i = 0.97955$, which describes the incident beam direction normal to surface). Due to discretization this corresponds to a conical aperture angle of about ± 11.6° for the incident solar radiation flow $q_{in,sol}$, which appears in a reasonable range for realistic solar absorber configurations.

The thermal radiation from the environment (assumed ambient air temperature $T_{env,in}$) is introduced as a diffuse contribution to the incoming ordinates intensity.

$$I_i^+(x = 0) = \delta_{i4} \cdot \frac{q_{in,sol}}{\varpi_i' \cdot \mu_i} + \frac{\sigma \cdot T_{env,in}^4}{\pi} \tag{29}$$

The convective losses to the environment at the absorber front side are considered by applying a constant convective heat transfer coefficient $h_{ambient}$ to model forced and natural convection processes at the irradiated side of the receiver (see Eq. (30)). When assuming no-wind conditions, hence pure natural convection phenomena, a typical value for $h_{ambient}$ is 8 W/(m^2 K). This value has been obtained from a natural convection Nusselt number correlation for a vertical plate [52].

$$\dot{Q}_{con} = A_{receiver} \cdot h_{ambient} \cdot (T_{surface} - T_{env,in}) \tag{30}$$

It must be noted that there is no natural convection present when considering a vertical absorber matrix through which air is aspirated from the ambient, as the inlet velocity dominates air movement close to the absorber surface and no natural convection profile can establish. However, due to spillage of the incident radiation on radiation shields at the frame of the absorber, the surrounding hot surfaces are expected

to induce natural convection. Additionally, at modular receivers hot recirculation air exits between receiver cups (see Fig. 2) and only about 40% [13] of that air stream is aspirated again by the receiver. The remaining hot air stream is mixed with ambient air and will move upwards the receiver front surface enhancing natural convective phenomena. Of course, this could be studied in detail by a thorough CFD analysis at receiver scale, which is however out of scope for the present work. However, considering that the convective heat loss (for non-wind conditions) is very small compared to the dominant radiative heat loss, the authors believe that Eq. (30), used with a typically small natural convective heat transfer coefficient, forms a reasonable modeling approach.

The choice of a suitable radiation boundary condition at the absorber outlet in the 1D approach is not trivial. Though it depends on the specific receiver design, for a general trend analysis of absorber material influences, a reasonably idealized approach can be used. A typical assumption is to consider the absorber housing at the absorber outlet side as a well-insulated, absorbing black cavity, emitting back on the absorber outlet face with a diffusive thermal equilibrium radiation, corresponding to an effective housing solid temperature. This temperature reaches a specific value $T_{housing}$, determined by the balance of the thermal sources (absorption of absorber outlet radiation, convective heat transfer with hot absorber outlet air) and the thermal losses to the environment. In an ideal (upper limit) case (no loss to environment, radiative interaction dominates wall heating) all radiation from the absorber outlet is fully absorbed at the housing walls and emitted back to it as diffusive equilibrium thermal radiation (temperature $T_{housing,ideal}$), resulting in a zero net radiation flow. This corresponds to the reference boundary condition at absorber outlet position ($x = h_{abs}$):

$$I_i^-(x = h_{abs}) = \frac{\sigma}{\pi}\cdot T^4_{housing,ideal} = \frac{\sigma}{\pi}\cdot \sum_k^n \frac{1}{\sigma}\cdot \varpi'_k\cdot \mu_k \cdot I_k^+(h_{abs}) \tag{31}$$

That rear boundary condition is selected as the reference model setup for the general 1D-DO model analyses, for the model comparison study, and for the optimization analysis described in Section 5.

In real systems, the effective housing temperature will take lower values ($T_{\text{housing}} < T_{\text{housing,ideal}}$), due to heat losses to the environment – resulting in a nonzero radiation flow balance at the absorber outlet ($|I^+| > |I^-|$). An alternative, non-adiabatic approach describes a – more or less hypothetical – situation, where convective heat transfer from hot outlet air is the dominant mechanism for housing wall temperature build-up. In that case, the cavity wall temperature is estimated to be equal the absorber outlet gas temperature value:

$$I_i^-(x = h_{abs}) = \frac{\sigma}{\pi}\cdot T^4_{\text{gas}}(x = h_{abs}) \tag{32}$$

That assumption is not related to a specific receiver design of practical importance and does neither represent a lower limiting case (since conductive insulation losses may result in an even lower cavity wall temperature). This boundary case (“boundary case B”) is only relevant for thin absorber layers, where the incident solar radiation is not fully absorbed and thermal equilibrium between absorber and air flow is not reached. This modified boundary condition showed slightly better spreading of the 7 validation cases (see Table 1) and thus seems to better fit the specific experimental setup. The impact is however small and does not change the predicted performance ranking of the investigated cases.

The simplified absorber model (with imposed radiation model), on the other hand, is not sensitive enough to justify this additional effort for the boundary condition at the rear. Here, the rear end of the absorber solid (1-D effective diffusion model) is assumed as adiabatic. There is no heat transfer between absorber back side and the internal receiver air ducts. The boundary condition on the front side considers convective losses as discussed above, and thermal radiation losses according to Eq. (33), considering the ambient as black body (see Fig. 4).

$$\dot{Q}_{rad} = A_{receiver}\cdot\sigma\cdot\varepsilon\cdot(T^4_{surface} - T^4_{env,in}) \tag{33}$$

The thermal emittance ε is taken as 0.8 [59].

3.5. Multi-layer model configuration

Recent publications [29,30] have shown that a variable and decreasing porosity in direction of air flow can be very favorable in terms of thermal efficiency of the volumetric absorber. For this reason, also multi-layer or stacked foam absorber configurations will be studied. Fig. 7 shows a typical example having porosities of 91, 85 and 81%.

The multi-layer absorber models are identical to the single-layer models as described above, except that the parameters can be defined for each layer separately, and that the solar irradiance exiting the previous layer is the initial irradiance level of the next one. Furthermore, the fluid enthalpy exiting the previous layer is the inlet enthalpy of the subsequent one. In the simplified absorber model, the 1-D solid structure diffusion models of each layer are coupled providing an effective thermal conductivity according to Eq. (15), providing geometrical mean parameters of both adjacent layers. In the detailed DO absorber model, no specific boundary conditions are used between layers, only the natural boundary conditions (continuity) for the radiative problem, resulting from the PDE structure of the problem.

3.6. Model implementation and simulation environments

The presented 1D-DO absorber model has been implemented in the Multiphysics Finite Element platform FlexPDE. All balances, correlations and declarations are user specific definitions. Model geometry, material properties and loads are fully parametrized. Foam property correlations are freely selectable by the user. It is therefore very easy to adapt the model to different geometries, loads and foam property models. Model results were automatically exported to ASCII tables and bitmap files. It is possible to run the model from command line with ASCII input and output files, offering a simple interface to external optimization software, as for instance Mathematica.

Table 1
Sample data for tests at solar simulator.

Case	Cell density (PPI)	Open porosity (–)	Sample thickness (mm)	Cell diameter (μm)	Window diameter (μm)	Strut thickness (μm)	Incident power (W)
1	30	0.809	15	1419	441	285	760
2	30	0.777	15	1365	443	303	760
3	10	0.813	15	4200	1382	784	760
4	10	0.79	15	4069	1545	881	760
5 Layer 1	10	0.84	5	4226	1321	746	760
5 Layer 2	20	0.809	5	2665	1013	486	
5 Layer 3	30	0.741	5	1361	504	310	
6 Layer 1	10	0.84	5	4226	1321	746	760
6 Layer 2	30	0.76	10	1344	445	301	
7 Layer 1	10	0.833	10	5403	1700	765	760
7 Layer 2	30	0.741	5	1361	504	310	

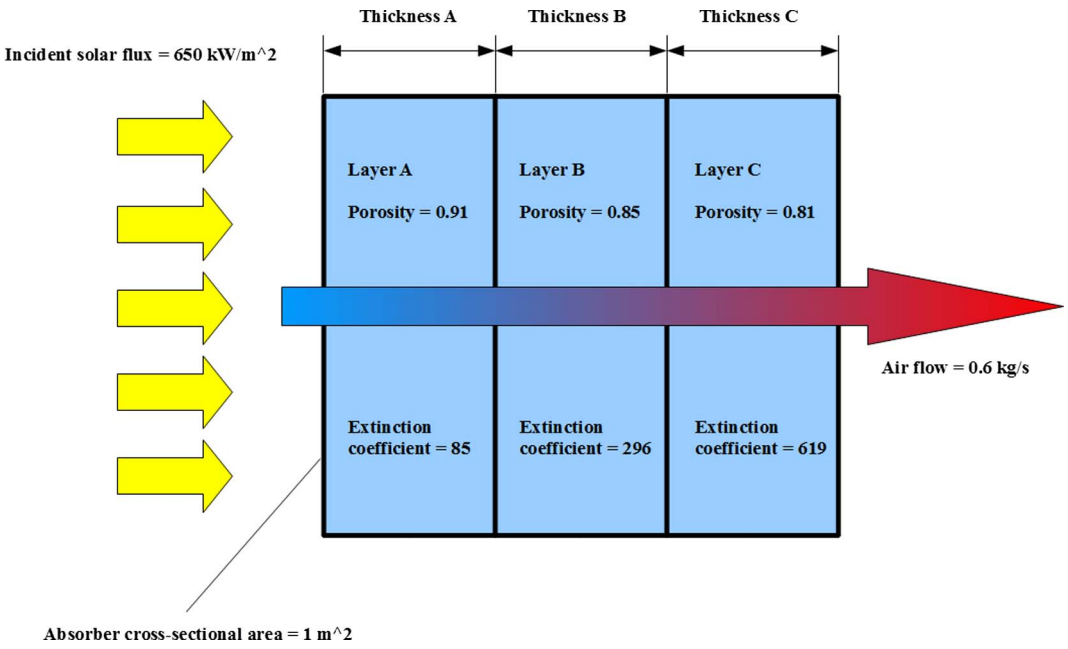

Fig. 7. Multi-layer or stacked foam configuration.

The simplified absorber model (with imposed radiation model) has been implemented applying the modeling language Modelica [60]. Modelica is a multi-purpose physical system modeling language and has been developed in an international effort in order to unify already existing similar modeling approaches and to enable developed models and model libraries to be easily exchanged. The absorber model builds upon the free Modelica Standard Library (MSL) [61] introducing new model components regarding solar and thermal radiation modeling and heat transfer. The developed Modelica code has been simulated applying a state-of-the-art commercial Modelica tool, applying its differential-algebraic system solver DASSL [62,63]. Although the model is formulated in fully transient mode, only steady-state simulation results are discussed in this work.

Finally, it should be noted that the models have been checked for grid independence by performing a reference simulation with different numbers of nodes. For example, about 100 control volumes for an absorber of about 4 cm of depth resulted to be a good choice.

3.7. Simulation results comparison – detailed DO model (IKTS) vs. simplified absorber model (CENER)

For both model types, a wide variety of accessible quantities allows deep physical insight into the absorber mechanisms. Exemplary results of both models are displayed in Figs. 8–14. The selected foam parameters correspond to the values of Case 1 for the single layer absorber and Case 5 for the multilayer absorber from Table 1. The loading conditions are chosen equivalent to the experimental set up described in Section 4 (incident radiation: 760 W, absorber area: 12.6 cm^2, air flow rate 3 kg/h).

Note that the displayed DO-model local net radiation flow (Fig. 12) includes thermal radiation flow contributions emitted from the foam to the environment, while the displayed imposed radiation model results only show incident radiation flow (thermal emission in that model emanates from solid surface only). The radiation flow level at the absorber inlet is only apparently higher for the simplified model.

The model results demonstrate the prominent importance of volumetric heat transfer coefficient h_v and incident radiation penetration depth (inverse extinction coefficient $1/K$) as the dominant influencing factors on absorber thermal efficiency: increasing heat transfer coefficient results in a stronger convective cooling of the foam near the solar irradiation surface and increasing penetration depth ($1/K$) shifts and distributes the absorbed heat of the solar radiation power to deeper and broader zones of the absorber. Both mechanisms result in a lower temperature level near the absorber surface, thereby reducing the thermal losses by emitted thermal radiation to the environment by the front surface, so increasing the absorber thermal efficiency. Both volumetric heat transfer coefficient and penetration depth/extinction coefficient are strongly related to foam structure parameters by complex correlations and show conflicting trends (increasing porosity as well as increasing cell size results in decreasing h_v but increasing $1/K$). The intention behind the multilayer foam configuration ("Case 5") in the example was to increase radiation penetration depth and thereby spreading absorption heat source over a broader volume in the foam, compared to the single layer Case 1. Though that was successfully reached (Fig. 12), a lower thermal efficiency was obtained for Case 5 (see difference in outlet temperatures in Figs. 8 and 9) due to the concurrent, dramatically decrease in the volumetric heat transfer coefficient from the choice of foam structural parameters for Case 5 compared to Case 1 (see Fig. 14).

Comparing the results of the DO (IKTS) and the simplified (CENER) model provided consistent trends and, in general, very similar results

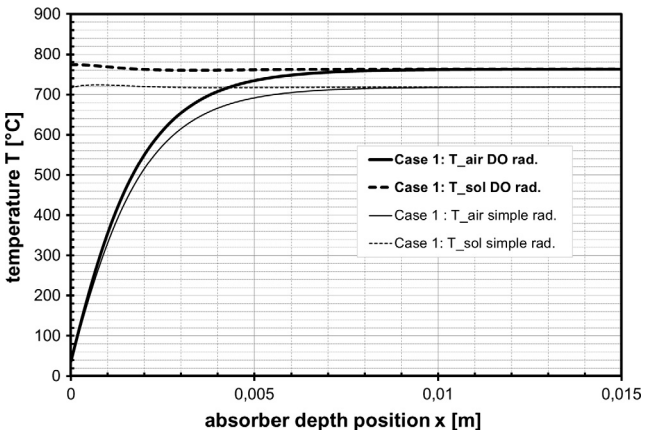

Fig. 8. Results from IKTS 1-D DO model (black) and the simplified 1-D CENER model (gray) for gas (solid) and solid (dotted) temperature vs. absorber depth position x for a 1 layer absorber ("Case 1", Table 1) configuration.

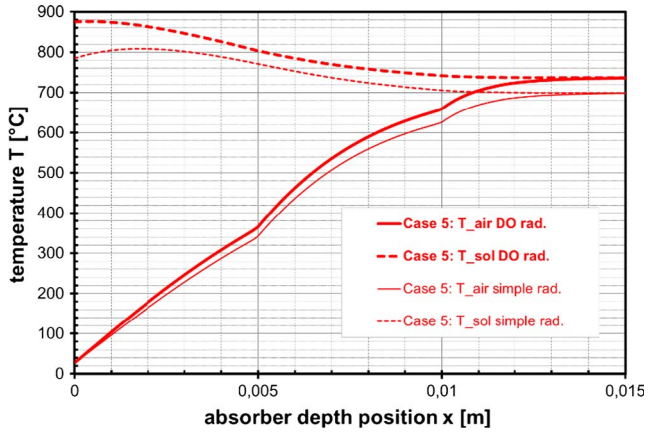

Fig. 9. Results from IKTS 1-D DO model (red) and the simplified 1-D CENER model (light red) for gas (solid) and solid (dotted) temperature vs. absorber depth position x for a 3 layer absorber ("Case 5", Table 1) configuration. (For interpretation of the references to colour in this figure legend, the reader is referred to the web version of this article.)

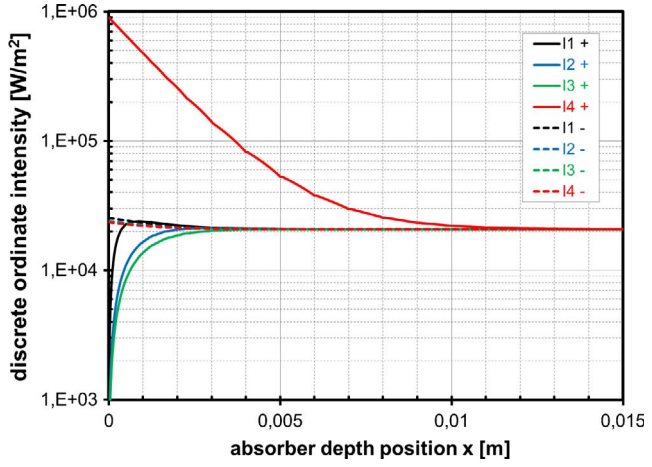

Fig. 10. Results from IKTS 1-D DO model for the discrete ordinate radiation intensities vs. absorber depth position x for the 1 layer configuration ("Case 1", Table 1).

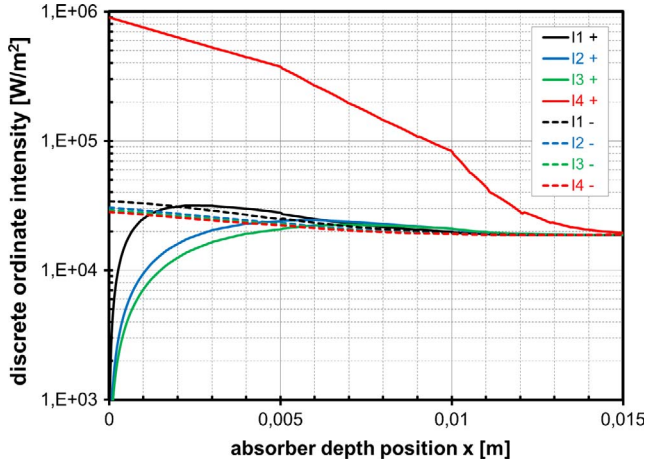

Fig. 11. Results from IKTS 1-D DO model for the discrete ordinate radiation intensities vs. absorber depth position x for the 3 layer configuration ("Case 5", Table 1).

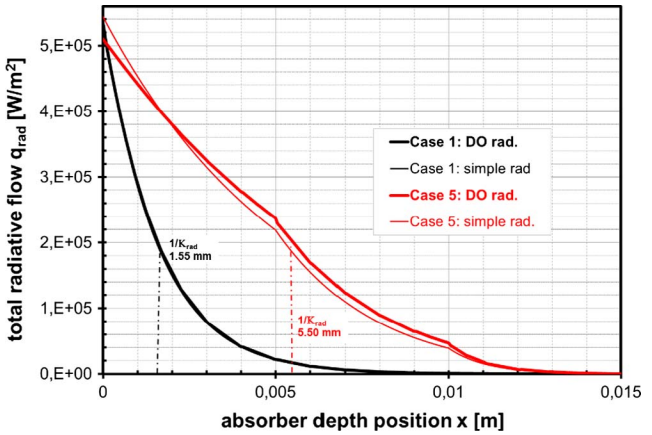

Fig. 12. Results from IKTS 1-D DO model (black: "Case 1", red: "Case 5", Table 1) and the simplified 1-D CENER model (gray, light red) for the net radiation power flow q_{rad} (corr. to Eq. (6)). (For interpretation of the references to colour in this figure legend, the reader is referred to the web version of this article.)

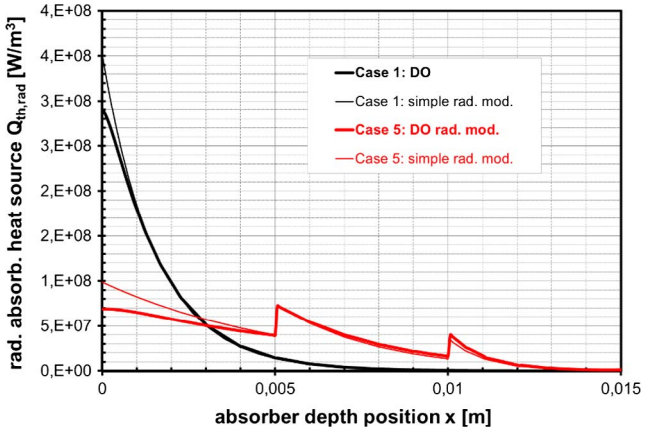

Fig. 13. Results from IKTS 1-D DO model (black: "Case 1", red: "Case 5") and the simplified 1-D CENER model (gray, light red) for the absorbed radiation volumetric thermal power source (corr. to Eq. (5)). (For interpretation of the references to colour in this figure legend, the reader is referred to the web version of this article.)

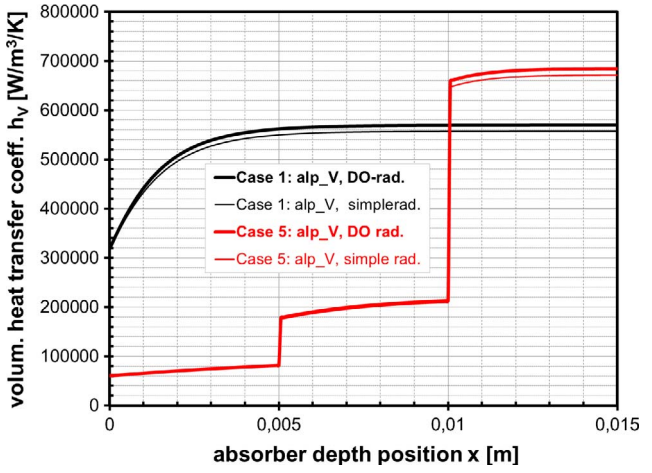

Fig. 14. Results from IKTS 1-D DO model (black: "Case 1", red: "Case 5") and the simplified 1-D CENER model (gray, light red) for volumetric heat transfer coefficient $h_v = h_f S_v$. (For interpretation of the references to colour in this figure legend, the reader is referred to the web version of this article.)

for all quantities. Nevertheless, the absolute level of the predicted air outlet temperature was significantly (20–50 K) lower for the simplified model in the analyzed cases. From a detailed comparison of the model results for various physical quantities there were found two sources for the differences:

- The simplified model, with its idealized assumption of a smooth solid surface, reflects that share of the incident solar irradiation that corresponds to the reflectivity $(1 - \varepsilon)$ of the bulk foam material, while the DO model reflects a significantly lower share of the incident radiation, due to the fact that the homogenized correlations of the DO approach also inherently account for internal multiple scattering and absorption interactions in the volume of the foam. The effective reflectivity of the foam is therefore lower than the bulk material value and conversely the effective emissivity higher. Accordingly the amount of absorbed solar irradiation power is higher in the DO-model.
- While in the simplified model thermal radiation losses from the surface are emitted with an intensity corresponding to the foam "surface temperature", thermal radiation in the DO model (and in reality) is emitted from a finite volume zone in the foam beneath the surface where the local temperature distribution may significantly differ from that on the surface. That may result in over- or underestimating thermal radiation losses depending on temperature distribution in the surface zone. The use of an "effective emission temperature" value obtained from averaging T^4 over the penetration depth zone (extension about 1/K) could improve the validity of the simplified model.

The following recommendation for an appropriate choice and application of the two model variants can be given. The DO model variant is well suited for detailed, locally resolved investigations of foam material parameter influences on volumetric absorber operation and performance. Its more realistic representation of the semitransparent character of the absorber foam reflects itself in appreciable effects on absorber operation. The simplified model with imposed radiation provides slightly different, but comparable results. Since it is implemented in Modelica code, it can be easily integrated into simulator applications on full system level, considering the interactions with other components (heliostat field, heat exchangers, thermal energy storage, power conversion unit) and the dynamic behavior of the system. It nicely represents absorber integral characteristics and delivers a satisfying quantitative description in a full system simulation context.

4. Experimental

In order to check the numerical models for consistency, they have been compared with experimental data, obtained at a 4 kW solar simulator (see Refs. [28,29]).

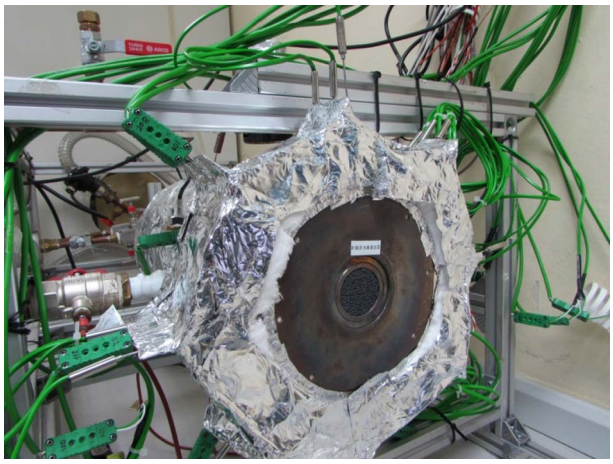

Fig. 16. Receiver unit with foam absorber placed in the receiver tube.

4.1. Description of the experimental facility

The facility is composed by four sub-systems designed for the lab-scale evaluation of different volumetric-receiver samples [28] (see Fig. 15):

- A 4 kW solar simulator made up of a xenon lamp (7) and an elliptic concentrator (8).
- A receiver sub-system (2) where the different volumetric absorbers (1) are placed. The absorber temperature is monitored by 24 K-type thermocouples distributed in six sections, 1 T-type thermocouple, 3 PT100 surface sensors and an infrared camera.
- A helical air-water heat exchanger sub-system (4) equipped with 4 PT100 sensors, 1 T-type thermocouple, a water mass flow-rate measurement, and a pump.
- An extraction sub-system with 2 PT100 sensors, an air mass flow-rate measurement (5), and a blower (6).

The test loop is shown in Fig. 15. The volumetric absorber sample (1) is mounted at the inlet of the air duct/receiver pipe (2). The ambient air is forced through the experimental circuit by the blower (6). In particular, the air is forced through the absorber sample (1), the receiver pipe (2), the air/water heat exchanger (4) and the flow meter (5). The absorber sample (1) is irradiated by concentrated light of a xenon lamp (7). The heat exchanger and the receiver unit are insulated (3) in order to keep thermal losses as low as possible.

Fig. 16 shows the receiver unit equipped with a foam absorber and thermocouples. Fig. 17 shows the absorber sample in detailed view. This absorber sample corresponds to Case I of Table 1.

The test of each sample took between 6 and 8 h. During this time the

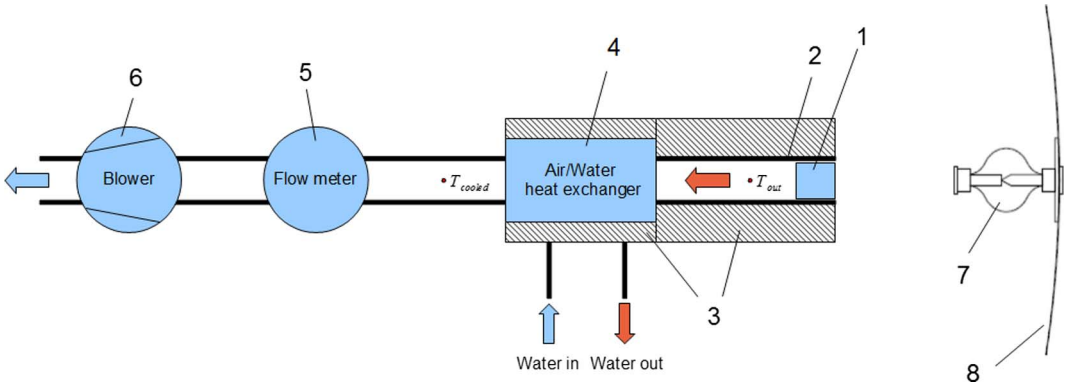

Fig. 15. Scheme of experimental facility.

Fig. 17. Close view of the absorber sample placed in the receiver tube (Case I according to Table 1).

irradiation was kept constant. To achieve various air outlet temperatures, the mass-flow was varied four times. At the start-up, the highest value (10 m^3/h) was set to avoid thermal shocks. After each step the mass flow was kept constant between 90 and 120 min to reach thermal equilibrium. The reason for this long period is that despite the air achieved the steady state quite quickly, the water of the heat exchanger needed more time to get steady conditions. Once the steady state was reached, the temperatures and the radiation data were taken to characterize this steady state period. After 4 steps the lowest mass flow (4 m^3/h) was set with the corresponding "hottest" operating point. Then, each sample is tested at least three more times to demonstrate a general repeatability of the efficiency measurement. For the different measurements carried out, the K-type thermocouples used had a maximum error of 1.5 °C and the PT100 sensors used in the heat exchanger had a maximum error in the working range of less than 0.25 °C.

Table 2
Comparison between experiment and simulation (CENER simplified model) – incident power on absorber: 760 W.

Case	Mass flow rate (kg/h)	T room (°C)	T out exp. (°C)	Tout sim (°C)	Error abs. (°C)	Error rel. (%) based on temp. diff. across absorber
1	10.3	25.0	277.0	256.7	20.3	8.1
1	8.0	25.0	335.0	319.3	15.7	5.1
1	5.6	27.0	443.0	434.0	9.0	2.2
1	3.4	27.0	629.0	655.4	26.4	4.4
2	10.1	23.0	269.0	260.4	8.6	3.5
2	7.8	25.0	330.0	325.8	4.2	1.4
2	5.5	27.0	427.0	439.9	12.9	3.2
2	3.3	28.0	601.0	668.5	67.5	11.8
3	10.0	26.0	260.0	249.6	10.4	4.4
3	7.7	27.0	315.0	310.3	4.7	1.6
3	5.5	28.0	401.0	409.6	8.6	2.3
3	3.3	29.0	563.0	614.1	51.1	9.6
4	10.2	24.0	259.0	249.2	9.8	4.2
4	7.7	26.0	317.0	314.9	2.1	0.7
4	5.4	27.0	409.0	421.7	12.7	3.3
4	3.3	28.0	580.0	621.8	41.8	7.6
5	10.2	28.0	274.0	256.7	17.3	7.0
5	7.8	28.0	330.0	322.0	8.0	2.7
5	5.7	28.0	422.0	419.0	3.0	0.8
5	3.4	28.0	608.0	637.7	29.7	5.1
6	10.2	25.0	269.0	256.2	12.8	5.3
6	7.8	26.0	333.0	322.2	10.8	3.5
6	5.6	27.0	428.0	426.8	1.2	0.3
6	3.4	27.0	614.0	642.1	28.1	4.8
7	10.3	26.0	271.0	248.5	22.5	9.2
7	7.9	27.0	330.0	311.5	18.5	6.1
7	5.6	27.0	425.0	416.6	8.4	2.1
7	3.4	28.0	605.0	625.7	20.7	3.6

4.2. Samples tested and comparison of experimental and numerical data

Small foam absorber samples with 40 mm in diameter have been prepared by IKTS. Varied parameters are nominal cell density, porosity and sample thickness. Table 1 displays the sample data for the 7 cases tested. Cases 1 to 4 are single-layer configurations. Cases 6 and 7 are double-layer configurations. Case 5 is a triple-layer configuration.

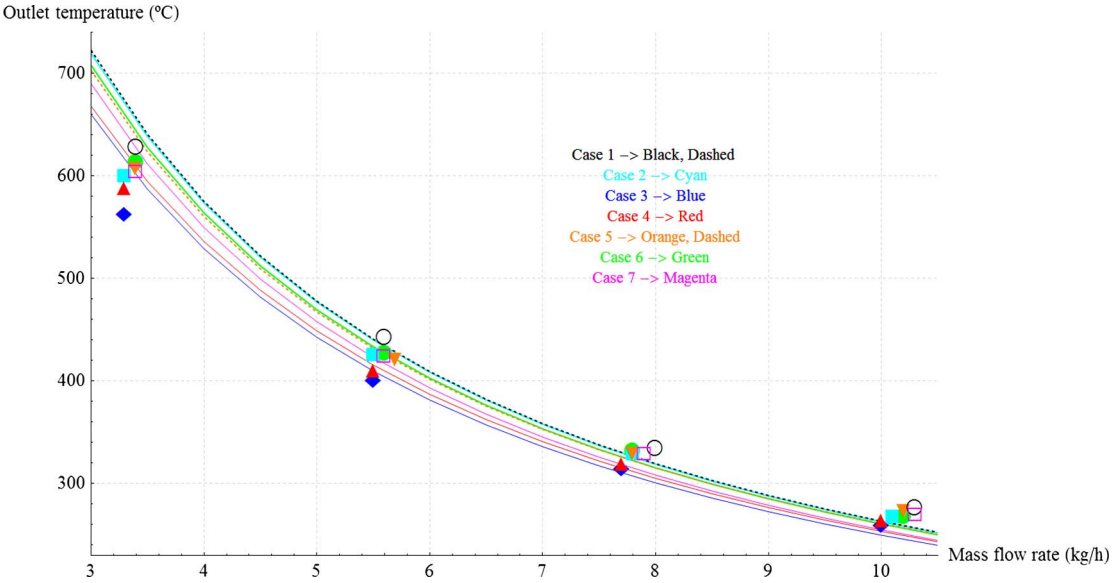

Fig. 18. Comparison of simulated (CENER simplified model) absorber performance (lines) and experimental data (symbols).

Table 3
Absorber sample ranking.

Ranking	Experiment (low flow rates)	CENER simplified model	IKTS DO model
1	Case 1 – single layer	Case 1 – single layer	Case 1 – single layer
2	*Case 6 – double layer*	Case 2 – single layer	Case 2 – single layer
3	**Case 5 – triple layer**	*Case 6 – double layer*	*Case 6 – double layer*
4	*Case 7 – double layer*	**Case 5 – triple layer**	**Case 5 – triple layer**
5	Case 2 – single layer	*Case 7 – double layer*	*Case 7 – double layer*
6	Case 4 – single layer	Case 4 – single layer	Case 4 – single layer
7	Case 3 – single layer	Case 3 – single layer	Case 3 – single layer

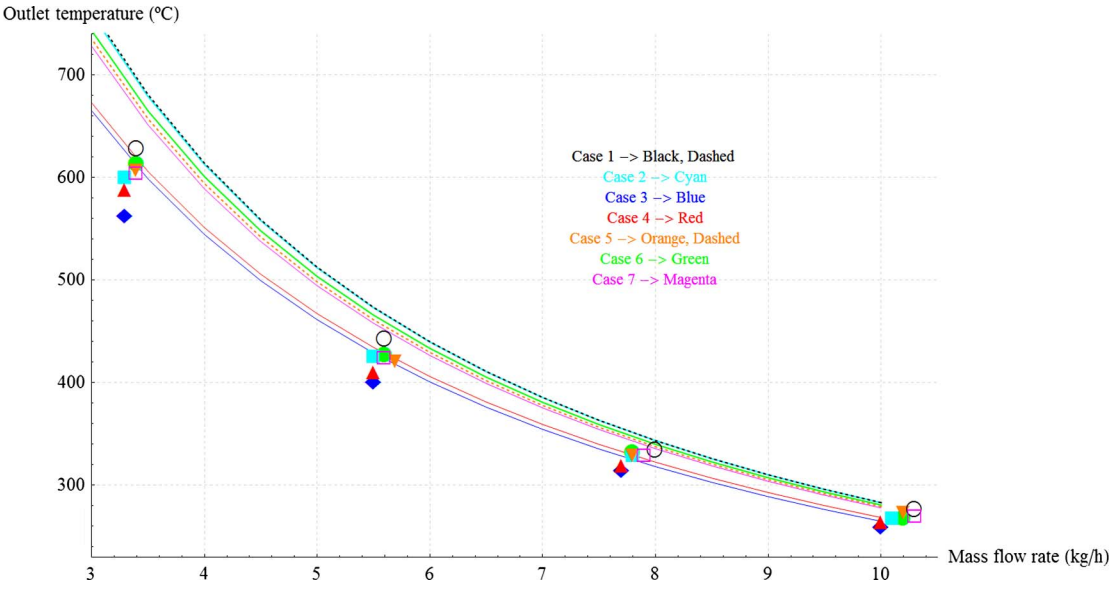

Fig. 19. Comparison of simulated (IKTS DO model) absorber performance (lines) and experimental data (symbols).

4.2.1. 1-D Modelica model (CENER)

Fig. 18 compares simulation results (lines) with the experimental data obtained (symbols). In this case, the simulation model used is the 1-D Modelica model developed by CENER. The model has been evaluated at different mass flow rates for each of the cases as outlined in Table 1. As can be seen in the plot, the simulations agree well with the experimental data. The relationship between flow rate and outlet temperature is captured well (11.8% max. rel. error, see Table 2).

As can be seen from the experimental data for low flow rates, Case 1 is the best configuration, followed by Case 6, 5 and 7, which are almost on the same level. Next is Case 2, followed by Case 4. Case 3 is the configuration with the worst performance. It is interesting to note that this sequence is also reproduced by the model for the single-layer configurations (see Fig. 18) and the multi-layer configurations, separately seen (see Table 3). The performance of the triple-layer configuration, Case 5, is very similar to Case 6.

4.2.2. 1-D DO model FlexPDE (IKTS)

Also the simulation results of the more detailed discrete ordinate absorber model have been compared to the experimental ones. Fig. 19 shows results for the assumption of boundary case B (effective temperature of the housing pipe at the absorber outlet is equal to the gas temperature), which has shown to best fit the experimental data, especially for the highly porous, low PPI foam test samples (Case 3, 4), where a significant part of the incident radiation passes through the absorber layer, due to the sample's small total thickness (15 mm). In the specific test set-up, that directed part of radiation energy flow may be absorbed at the cooled end (heat exchanger) of the housing pipe and the housing "cavity" will not reach the state of ideal adiabatic equilibrium (effective temperature $T_{housing,ideal}$). However, also the adapted assumptions for the 1D discrete ordinate model (boundary case B) predict a consistently higher temperature level than observed in the experiments. Those differences can be easily explained by additional thermal losses (conduction through insulation and from component mounting) which are present in the real test set up.

Generally, higher outlet temperatures are achieved with the 1-D DO model, when compared to the 1-D model with simplified imposed solar radiation model. Reasons for that have been already discussed in Section 3.7. The maximum deviation from experimental data is obtained for Case 2 at low flow rates, with an absolute error of 108 °C (19% relative, based on the temperature difference across the absorber).

4.2.3. Summary

It must be emphasized that with both models the same ranking of the cases is obtained (see Table 3). It can be said that the simulations are consistent with experimental data. The maximum deviation observed is 14.3% for the CENER Modelica model (simplified imposed radiation), and 19% for the IKTS DO model. The higher deviations of the advanced model compared to the simplified model are expected to be of a more coincidental nature, i.e. a result from uncertain, additional thermal system losses of the real experimental set-up as already has been discussed. Nevertheless, the principal relationship between outlet temperature and mass flow rate is captured well. Also the same ranking of single-layer absorber samples is confirmed by the experiment and two different models (see Table 3). The ranking among the multi-layer configurations (Cases 5, 6 and 7) is also the same in the experiment and for two different models. However, the relative ranking between single and multi-layer configurations cannot be clearly confirmed, as experimental and simulation results differ. However, the multi-layer cases stay clearly below the winner, which is Case 1, a single-layer configuration.

Table 4
Realistic SSiC foam data set provided by IKTS.

Nominal cell density (PPI)	Cell diameter PU (μm)	Strut thickness PU (μm)	Strut thickness ceramic (μm)	Layer thickness ceramic coating (μm)	Cell diameter ceramic foam (μm)	Material porosity (–)	Foam density (g/cm^3)	Total porosity (–)	Strut core porosity (–)	Open cell porosity (–)	Specific surface area (m^2/m^3)
8	5062	420	553	133	4144	0.32	368	0.88	0.02	0.81	873
8	5062	420	773	353	3915	0.32	470	0.85	0.02	0.76	952
8	5062	420	912	492	3757	0.32	621	0.8	0.02	0.69	999
10	4300	543	733	190	3920	0.32	296	0.91	0.02	0.84	885
10	4300	543	760	217	3866	0.32	323	0.9	0.02	0.83	913
10	4300	543	787	244	3812	0.32	351	0.89	0.02	0.81	941
10	4300	543	814	271	3757	0.32	380	0.88	0.02	0.8	968
10	4300	543	841	299	3703	0.32	412	0.87	0.02	0.79	993
10	4300	543	868	326	3649	0.32	445	0.86	0.02	0.77	1017
10	4300	543	896	353	3594	0.32	479	0.85	0.02	0.75	1039
10	4300	543	923	380	3540	0.32	516	0.84	0.02	0.74	1060
10	4300	543	950	407	3486	0.32	554	0.82	0.02	0.72	1078
10	4300	543	977	434	3432	0.32	595	0.81	0.02	0.7	1095
10	4300	543	1004	461	3377	0.32	637	0.8	0.02	0.68	1109
10	4300	543	1031	488	3323	0.32	681	0.78	0.02	0.66	1121
15	3100	393	531	138	2825	0.32	299	0.91	0.02	0.84	1230
15	3100	393	550	157	2785	0.32	326	0.9	0.02	0.83	1270
15	3100	393	570	177	2746	0.32	354	0.89	0.02	0.81	1308
15	3100	393	590	197	2707	0.32	384	0.88	0.02	0.8	1345
15	3100	393	609	216	2668	0.32	415	0.87	0.02	0.78	1380
15	3100	393	629	236	2628	0.32	449	0.86	0.02	0.77	1413
15	3100	393	649	256	2589	0.32	484	0.85	0.02	0.75	1443
20	2300	293	381	88	2124	0.32	276	0.91	0.02	0.85	1608
20	2300	293	396	103	2095	0.32	302	0.9	0.02	0.84	1663
20	2300	293	411	117	2065	0.32	329	0.9	0.02	0.82	1716
20	2300	293	425	132	2036	0.32	358	0.89	0.02	0.81	1768
20	2300	293	440	147	2007	0.32	388	0.88	0.02	0.8	1817
20	2300	293	455	161	1977	0.32	420	0.87	0.02	0.78	1864
20	2300	293	469	176	1948	0.32	454	0.86	0.02	0.77	1908
20	2300	293	484	191	1919	0.32	489	0.84	0.02	0.75	1949
20	2300	293	499	205	1889	0.32	527	0.83	0.02	0.73	1987
20	2300	293	513	220	1860	0.32	566	0.82	0.02	0.71	2021
20	2300	293	528	235	1831	0.32	607	0.81	0.02	0.69	2051
20	2300	293	543	249	1801	0.32	650	0.79	0.02	0.67	2077
25	1800	231	300	69	1661	0.32	280	0.91	0.02	0.85	2061
25	1800	231	312	81	1638	0.32	306	0.9	0.02	0.84	2132
25	1800	231	323	92	1615	0.32	333	0.89	0.02	0.82	2200
25	1800	231	335	104	1592	0.32	362	0.89	0.02	0.81	2265
25	1800	231	347	116	1569	0.32	393	0.88	0.02	0.8	2328
25	1800	231	358	127	1546	0.32	425	0.87	0.02	0.78	2388
25	1800	231	370	139	1523	0.32	459	0.85	0.02	0.76	2444
30	1450	187	244	56	1338	0.32	283	0.91	0.02	0.85	2568
30	1450	187	253	66	1319	0.32	309	0.9	0.02	0.83	2655
30	1450	187	262	75	1300	0.32	337	0.89	0.02	0.82	2739
30	1450	187	272	84	1281	0.32	367	0.88	0.02	0.81	2821
30	1450	187	281	94	1263	0.32	398	0.87	0.02	0.79	2898
30	1450	187	290	103	1244	0.32	431	0.86	0.02	0.78	2972
30	1450	187	300	112	1225	0.32	465	0.85	0.02	0.76	3041
35	1200	156	195	39	1122	0.32	262	0.92	0.02	0.86	3006
35	1200	156	203	47	1106	0.32	287	0.91	0.02	0.84	3114
35	1200	156	211	55	1091	0.32	314	0.9	0.02	0.83	3220
35	1200	156	219	62	1075	0.32	342	0.89	0.02	0.82	3321
35	1200	156	226	70	1059	0.32	372	0.88	0.02	0.8	3419
35	1200	156	234	78	1044	0.32	404	0.87	0.02	0.79	3513
35	1200	156	242	86	1028	0.32	437	0.86	0.02	0.77	3601
35	1200	156	250	94	1013	0.32	472	0.85	0.02	0.76	3684
40	1035	136	183	47	940	0.32	318	0.9	0.02	0.83	3745
40	1035	136	190	54	927	0.32	346	0.89	0.02	0.82	3863
40	1035	136	197	61	913	0.32	377	0.88	0.02	0.8	3976
40	1035	136	203	68	899	0.32	409	0.87	0.02	0.79	4084
45	890	118	159	41	808	0.32	322	0.9	0.02	0.83	4371
45	890	118	165	47	796	0.32	352	0.89	0.02	0.81	4508
45	890	118	170	53	784	0.32	382	0.88	0.02	0.8	4639
45	890	118	176	59	772	0.32	415	0.87	0.02	0.78	4764
45	890	118	182	65	761	0.32	449	0.86	0.02	0.77	4881
45	890	118	188	71	749	0.32	486	0.85	0.02	0.75	4991

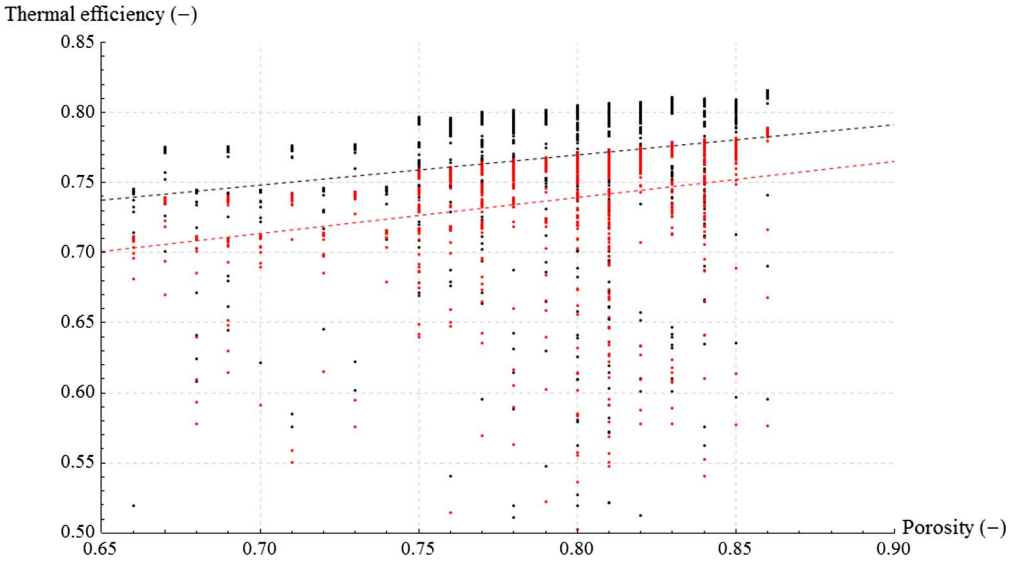

Fig. 20. Thermal efficiency over porosity of single-layer configuration – 0.6 kg/s (black), 0.5 kg/s (red). (For interpretation of the references to colour in this figure legend, the reader is referred to the web version of this article.)

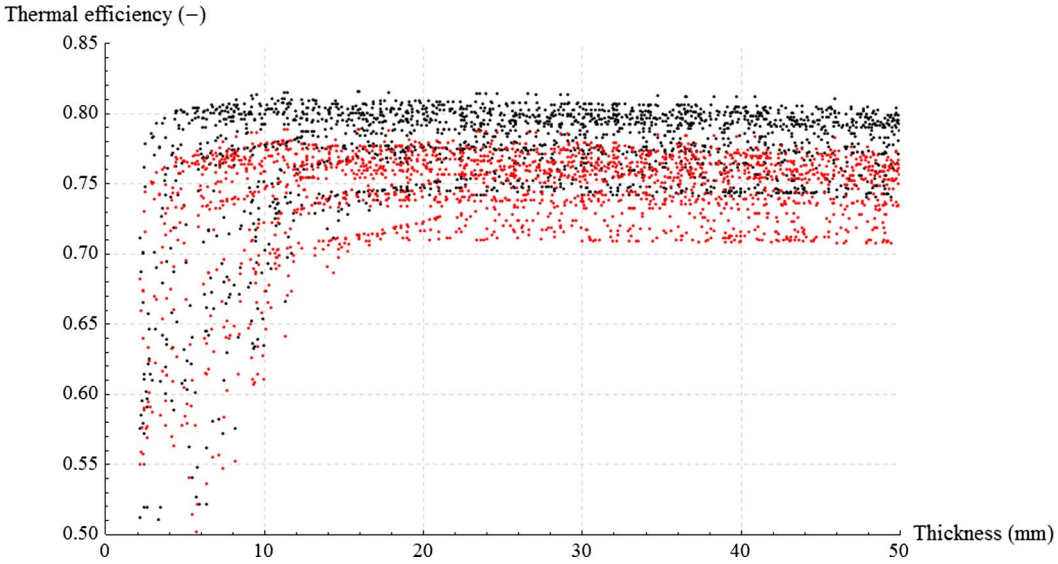

Fig. 21. Thermal efficiency over absorber depth of single-layer configuration – 0.6 kg/s (black), 0.5 kg/s (red). (For interpretation of the references to colour in this figure legend, the reader is referred to the web version of this article.)

Although there clearly exist some uncertainties, both in the experimental part and in the modeling approaches, the authors believe that the models are suitable for further parametric optimization runs, being able to give suggestions for foam parameters for future solar receiver designs.

5. Parametric study and optimization

Next, parametric optimization studies have been performed independently at two institutions (CENER and IKTS). In the following, the optimization results of both studies will be stated.

5.1. Parametric study on foam thermal efficiency at CENER (1-D Modelica model)

The aim of this section is to study the effect of all relevant foam parameters and to find most promising parameter combinations for highest possible thermal efficiencies. In order to do so, 2000 random parameter combinations have been produced for three absorber configurations, (i) a single-layer absorber, (ii) a double-layer absorber and (iii) a triple-layer absorber. The varied parameters have been layer depth, cell diameter, strut thickness, and porosity.

To guarantee foam parameter combinations that can also be manufactured (dependence on commercial availability of polymer foam, etc.) IKTS provided a set of foam parameters that represents realistic manufacturing ranges. This data set provides 66 different foam types (see Table 4 below). Model input parameters per foam type are strut thickness, cell diameter, and open cell porosity.

A random set of 2000 parameter combinations for each, the single-layer configuration, the double-layer configuration and the triple-layer configuration, have been generated, selecting randomly the layer type from Table 4 and layer thickness for each layer. The Modelica models were then run via calling them in a loop (Modelica scripting) using a state-of-the-art commercial Modelica tool. The cross-sectional area of the absorber has been set to 1 m^2 and the simulations have been run twice, applying for the first run a fixed mass flow boundary of 0.6 kg/s, and for the second run 0.5 kg/s. This has been done to achieve a variation in absorber outlet temperature, as the solar flux boundary was fixed at 650 kW/m^2.

From Figs. 20–24, the following can be observed for a single-layer configuration:

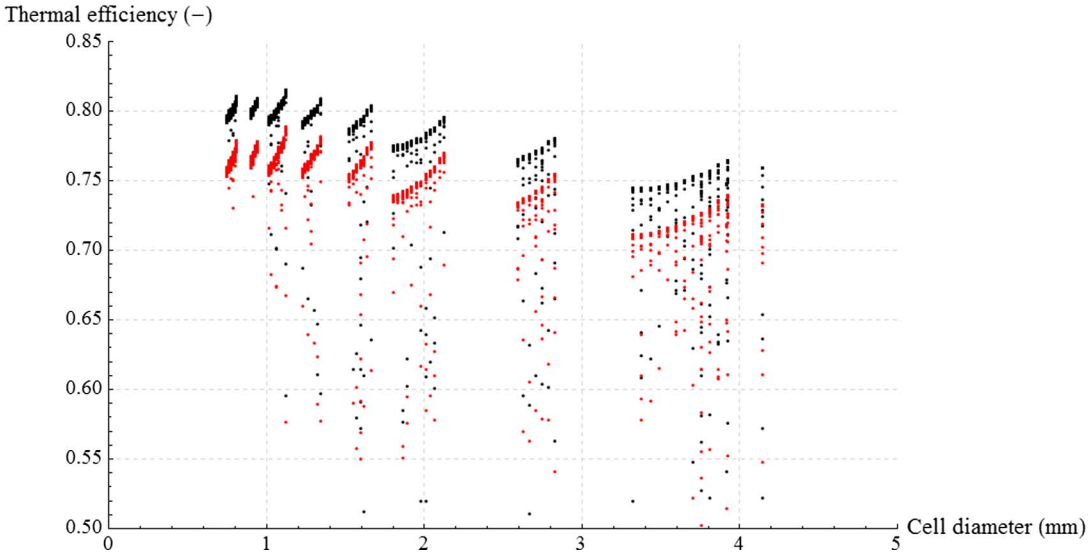

Fig. 22. Thermal efficiency over cell diameter of single-layer configuration – 0.6 kg/s (black), 0.5 kg/s (red). (For interpretation of the references to colour in this figure legend, the reader is referred to the web version of this article.)

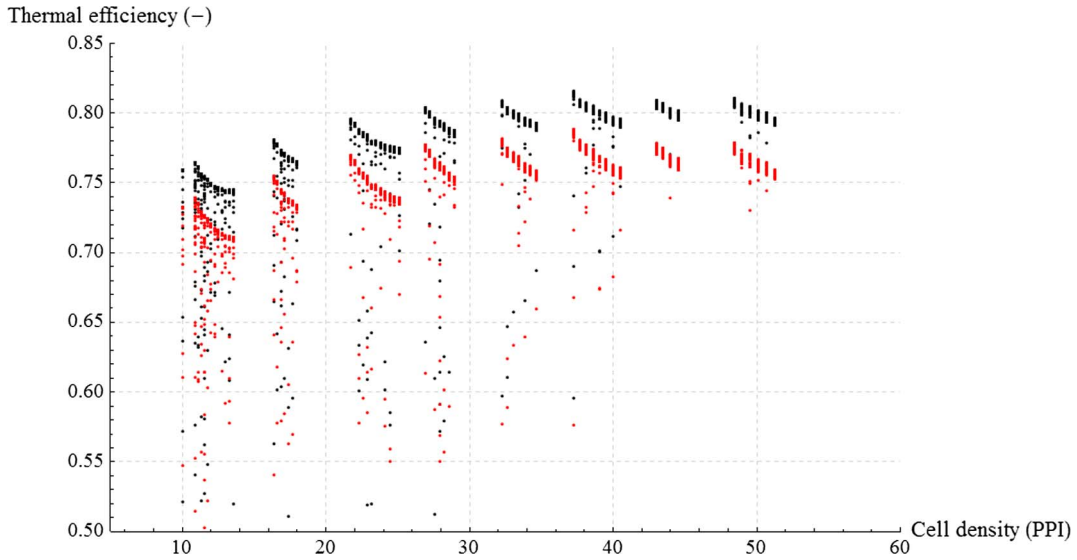

Fig. 23. Thermal efficiency over cell density of single-layer configuration – 0.6 kg/s (black), 0.5 kg/s (red). (For interpretation of the references to colour in this figure legend, the reader is referred to the web version of this article.)

- The efficiency largely depends on the porosity. The higher the porosity, the higher is the thermal efficiency (see dashed lines in Fig. 20 which represent the least-squares fit of the data points). Thus, the highest possible porosity should be chosen for future solar receiver designs.
- The layer thickness has a rather weak influence (Fig. 21). Nevertheless, it develops an optimum between 10 and 20 mm of layer thickness. Thus, from the point of thermal performance only, the absorber thickness shall not be larger than ≈20 mm. However, a higher thickness may be required due to mechanical aspects.
- Small cell diameters clearly show better performance. The optimum lies between 1 and 1.5 mm (see Fig. 22).
- The cell density (Fig. 23) develops a broad optimum between 30 PPI and 50 PPI.
- Finally, since the thermal efficiency is best for relatively small absorber thicknesses, the pressure drop keeps also relatively low for the best absorber configuration (see Fig. 24 and Table 5).

The best single-layer configuration of the 2000 random combination is given in Table 5 (Case I). Fig. 25 displays the corresponding temperature profiles for the 0.6 kg/s air mass flow boundary (solid lines), and the 0.5 kg/s air mass flow boundary (dashed lines). The black lines represent the temperatures of the foam nodes and the blue ones correspond to the temperatures of the fluid nodes. It can be seen that the so-called volumetric effect occurs, i.e. the air outlet temperature at the rear side of the absorber is higher than the foam temperature at the absorber front surface. The total longitudinal temperature difference (rear temperature minus front temperature) is about 97 °C for the 0.6 kg/s mass flow boundary, and about 140 °C for the 0.5 kg/s mass flow boundary. As can be observed in Fig. 25, most of the temperature gradient of the foam is accomplished within the first 5 mm of absorber depth. Thermal equilibrium between fluid and solid structure is achieved at around 10 mm of absorber depth.

The results obtained for a single-layer configuration have been compared with those coming from the parametric study for double and triple-layer absorber configurations. Fig. 26 shows the relationship between the thermal efficiency and the double-layer configuration's first layer (Layer A) porosity. As it was observed for the single-layer

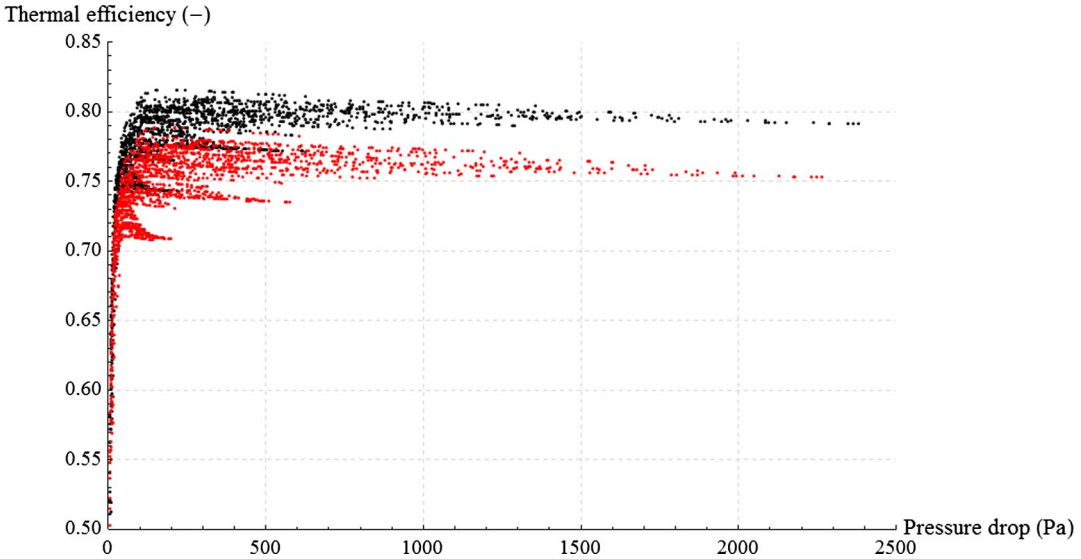

Fig. 24. Thermal efficiency over pressure drop of single-layer configuration – 0.6 kg/s (black), 0.5 kg/s (red). (For interpretation of the references to colour in this figure legend, the reader is referred to the web version of this article.)

Table 5
Best absorber configurations according to 1-D Modelica model.

Case – Layer	Cell density (PPI)	Thickness (mm)	Cell diameter (mm)	Strut diameter (mm)	Porosity (–)	Thermal efficiency (–) @ 845 °C	Thermal efficiency (–) @ 966 °C	Pressure drop (Pa) [57] @ 0.6 kg/s	Pressure drop (Pa) [57] @ 0.5 kg/s
I-1	37	15.9	1.122	0.195	0.86	0.816	0.788	178	169
II-1	37	5.9	1.122	0.195	0.86				
II-2	38	12.8	1.091	0.211	0.83				
II-Total		18.7				0.816	0.789	236	224
III-1	37	5.6	1.122	0.195	0.86				
III-2	21	9.5	2.095	0.396	0.84				
III-3	43	6.9	0.927	0.19	0.82				
III-Total		22				0.816	0.790	226	214

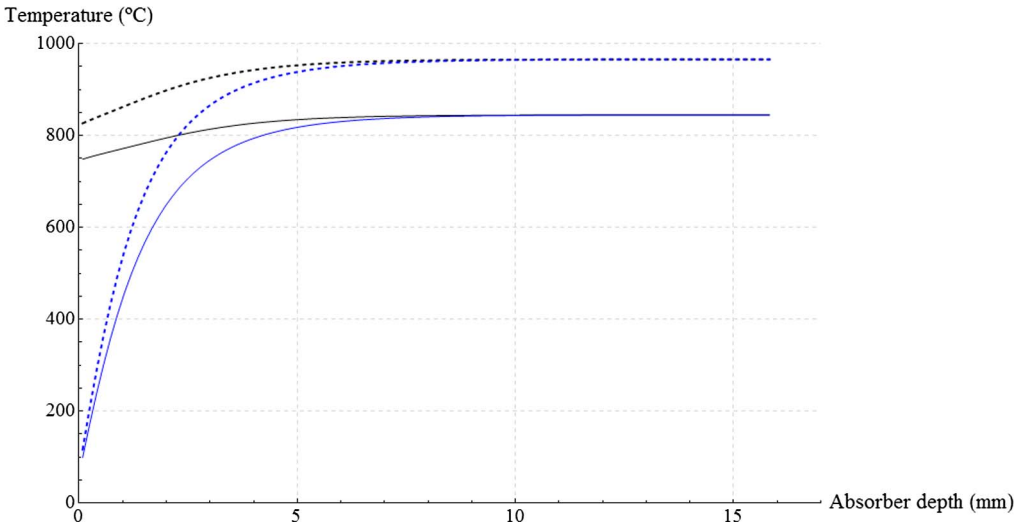

Fig. 25. Foam (black) and fluid (blue) temperature profiles of best single-layer configuration – 0.5 kg/s (dashed line), 0.6 kg/s (solid line). (For interpretation of the references to colour in this figure legend, the reader is referred to the web version of this article.)

cases, the thermal efficiency depends strongly on the porosity. The higher the porosity, the higher is the thermal efficiency. Again, the relationship is more pronounced for lower mass flow (0.5 kg/s) and higher outlet temperatures (red). For the second layer (Layer B) of the double-layer configuration, however, no relationship between porosity and thermal efficiency can be observed (see Fig. 27). The least-squares fits of the data points are practically horizontal lines (see dashed black and red line). Thus, only the properties of the first layer seem to determine the thermal performance of the solar absorber.

The same holds for the triple-layer configuration. Fig. 28 displays the relationship of the thermal efficiency and the triple-layer configuration's first layer (Layer A) porosity. Figs. 29 and 30 display the corresponding results for the second (Layer B) and third layer (Layer C), respectively.

For the sake of completeness, it must be emphasized that all scatter plots of the 2nd and 3rd layer show no relationship between thermal

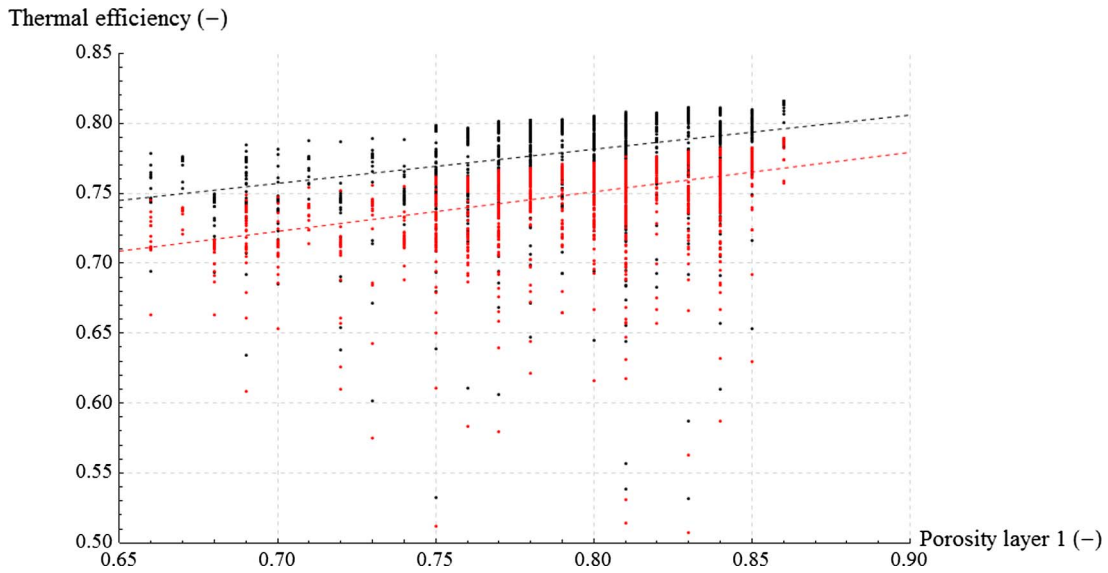

Fig. 26. Thermal efficiency over porosity of double-layer configuration (layer 1) – 0.6 kg/s (black), 0.5 kg/s (red). (For interpretation of the references to colour in this figure legend, the reader is referred to the web version of this article.)

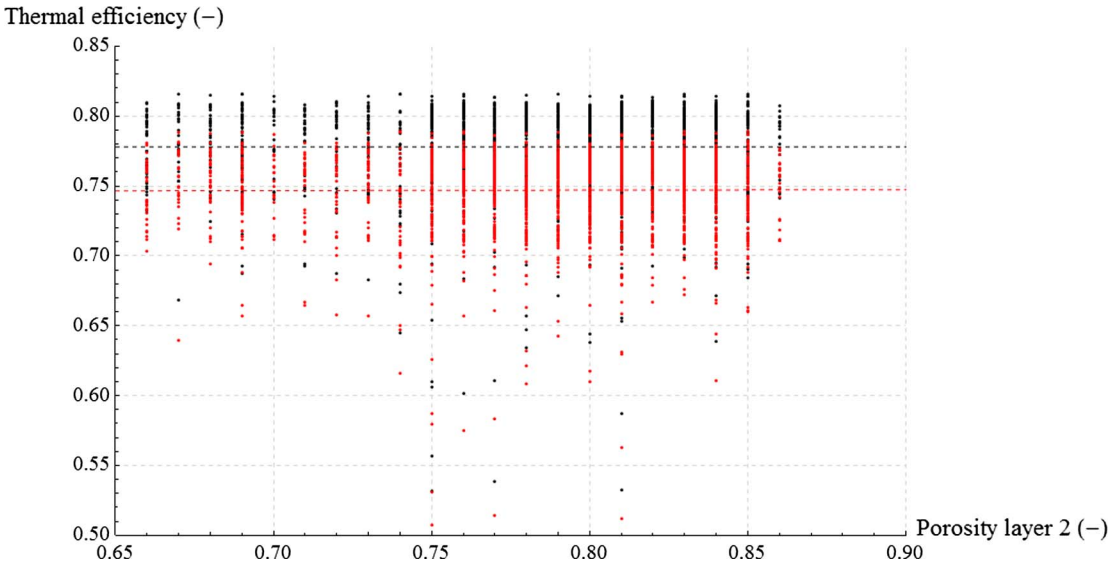

Fig. 27. Thermal efficiency over porosity of double-layer configuration (layer 2) – 0.6 kg/s (black), 0.5 kg/s (red). (For interpretation of the references to colour in this figure legend, the reader is referred to the web version of this article.)

efficiency and corresponding parameter (porosity, cell diameter, thickness and cell density). Thus, only the first layer's parameters are relevant for the solar absorber design regarding thermal efficiency.

The parameters of the best double-layer configuration are given in Table 5 (Case II). Fig. 31 shows the corresponding temperature profiles for the 0.6 kg/s air mass flow boundary (solid lines), and the 0.5 kg/s air mass flow boundary (dashed lines). The black lines represent the temperatures of the foam nodes, the blue lines represent the temperatures of the fluid nodes. Again, as observed at the single-layer configuration, the volumetric effect occurs.

Fig. 32 displays the temperature profiles for the best triple-layer configuration (Case III in Table 5). Very similar behavior is observed. The thermal non-equilibrium between solid and fluid phase is only dominant in the first layer. The properties of the second and third layer have a negligible effect on the thermal performance. Only the absorber pressure drop (see Table 5) and/or mechanical aspects can be influenced by the rear absorber layers. An interesting result is that all three configurations converge to about quite small optimum total absorber thickness, which is ≈16 mm for the single-layer configuration, ≈19 mm for the double-layer configuration, and ≈22 mm for the triple-layer configuration. Note that the standard honeycomb absorber has a thickness of about 50 mm. Thus, simulations show that the foam absorber can be designed thinner. Being the single-layer configuration also the thinnest option (lowest pressure drop), it is also most probably going to be the preferred option, simply due to simplicity of design and manufacturing. A double-layer configuration may be considered for purely structural/mechanical aspects if the single-layer foam should be too fragile.

5.2. Optimization of foam thermal efficiency at IKTS

Also the 1-D DO absorber model was applied in several optimization analysis runs at IKTS. So it took part in a benchmark analysis campaign (Triple Layer Absorber, random parameter combinations) together with the CENER 1-D model (described in Section 5.1) and provided comparable results. Although the absolute efficiency values obtained with the 1-D DO model were slightly different from the 1-D CENER model, due to its more detailed radiation description, it provided the same

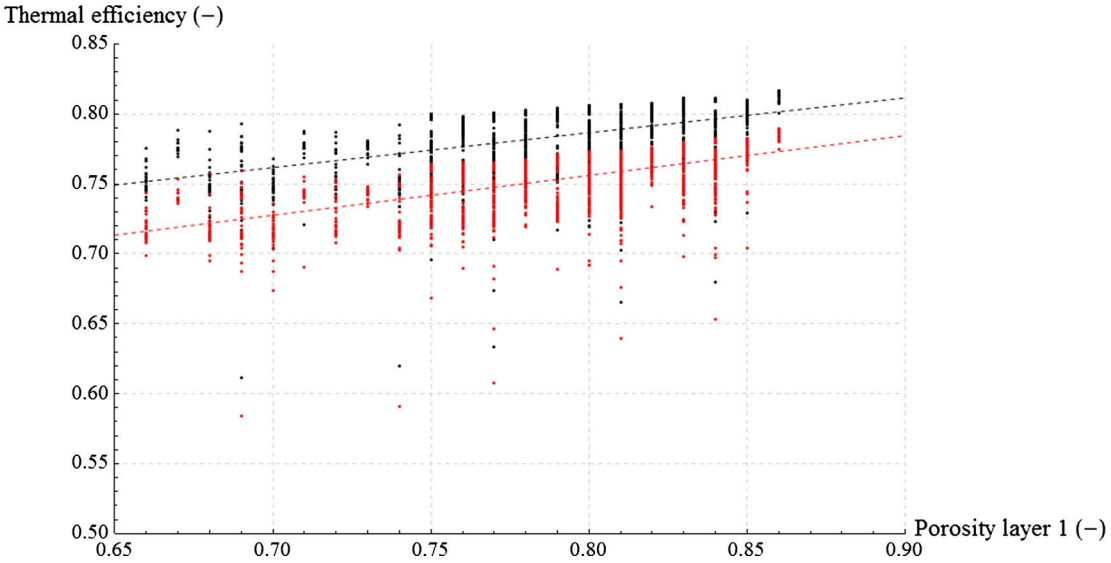

Fig. 28. Thermal efficiency over porosity of triple-layer configuration (layer 1) – 0.6 kg/s (black), 0.5 kg/s (red). (For interpretation of the references to colour in this figure legend, the reader is referred to the web version of this article.)

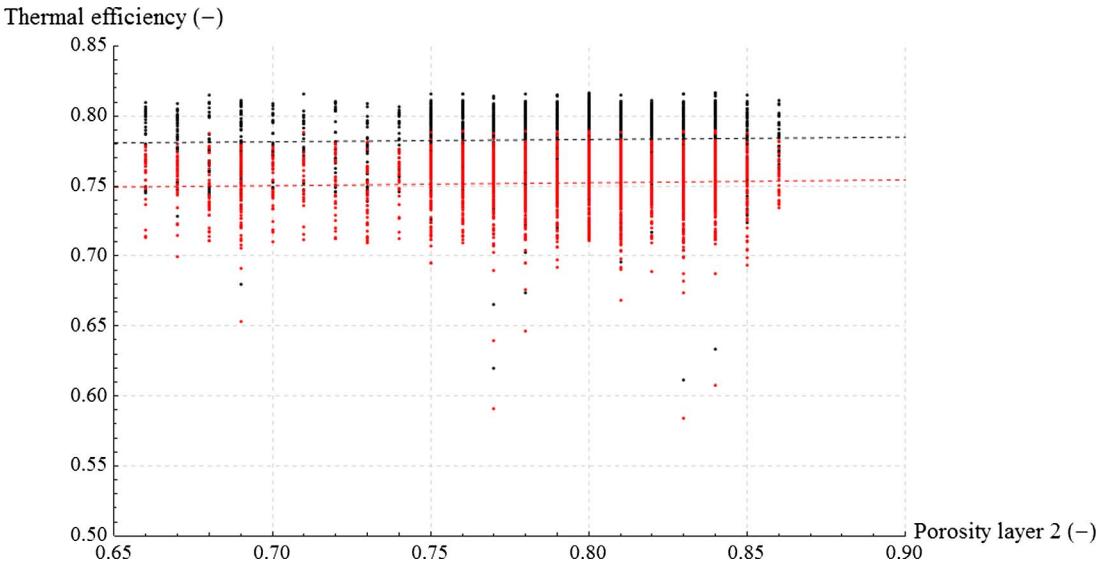

Fig. 29. Thermal efficiency over porosity of triple-layer configuration (layer 2) – 0.6 kg/s (black), 0.5 kg/s (red). (For interpretation of the references to colour in this figure legend, the reader is referred to the web version of this article.)

relative results: above a 1st layer minimum thickness, the influences of the 2nd and 3rd layer appear nearly irrelevant (at least in the range of the absorber performance optimum) with regard to the absorber thermal efficiency and, considering the first layer, an optimum exists for highest possible porosity values and a PPI value plateauing at a range of 40–60 for layer thicknesses $h_A > 25$ mm. For the triple-layer systems an alternative optimization analysis has been carried out, utilizing a Nelder-Mead Optimization Method [64] controlled by Wolfram Mathematica (NMaximize function) and applying the 1-D DO model via an external function call. This procedure also fully confirmed the above recommendations for *layer A* optimum properties: multiple runs of the optimization procedure with varied random starting values converged against the same above *layer A* property values, while *layer B* and *C* property results appeared arbitrary. Since both approaches and their results are fully comparable to the analyses at CENER, only a global summary of the results obtained has been included.

In a different, not stochastically based approach, we conducted a variation analysis for a double layer system on a regular grid of parameter variations for layer thickness (assuming a constant total absorber thickness $h_{tot} = 60$ mm), porosity (variation range top layer A: 0.8–0.93, bottom layer B: 0.6–0.9) and PPI (variation range layer A: 8–50, layer B: 20–60) of both layers. The thickness of the top layer was varied between $10\text{ mm} \leq h_A \leq 50\text{ mm}$. A total of 5400 parameter combinations had been computed. The regular parameter spacing allowed an interpolation and graphical visualization of the optimization results within Wolfram Mathematica. The thermal efficiency shows a continuous increase with porosity of the first layer and a broad plateau-like maximum for top *layer A* PPI, developing above values of about 40 PPI (Figs. 33 and 34). Above a thickness value of 20 mm, for the first layer nearly no further influence of thickness on absorber performance could be observed. In that range, bottom *layer B* properties showed no relevant influence on thermal efficiency of the system, as is illustrated for exemplary results in Figs. 34 and 35.

The conclusions of the optimization analyses with the 1-D DO model can be summarized as follows: the first layer completely dominates the absorber's thermal performance, its porosity should be chosen as high as possible, a broad performance plateau develops starting from PPI values at about 40, and thicknesses above 20 mm appear fully

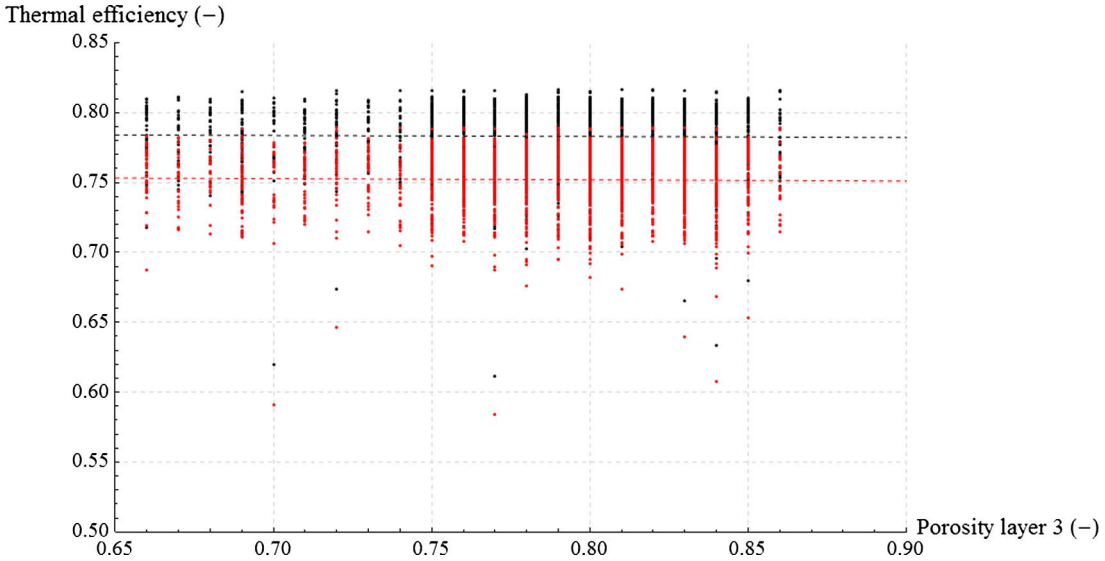

Fig. 30. Thermal efficiency over porosity of triple-layer configuration (layer 3) – 0.6 kg/s (black), 0.5 kg/s (red). (For interpretation of the references to colour in this figure legend, the reader is referred to the web version of this article.)

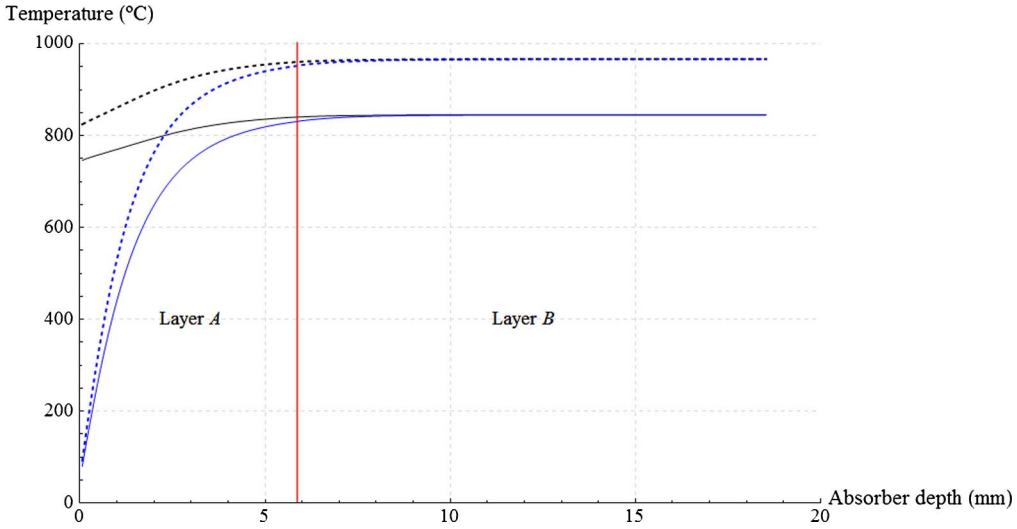

Fig. 31. Foam (black) and fluid (blue) temperature profiles of best double-layer configuration – 0.5 kg/s (dashed line), 0.6 kg/s (solid line). (For interpretation of the references to colour in this figure legend, the reader is referred to the web version of this article.)

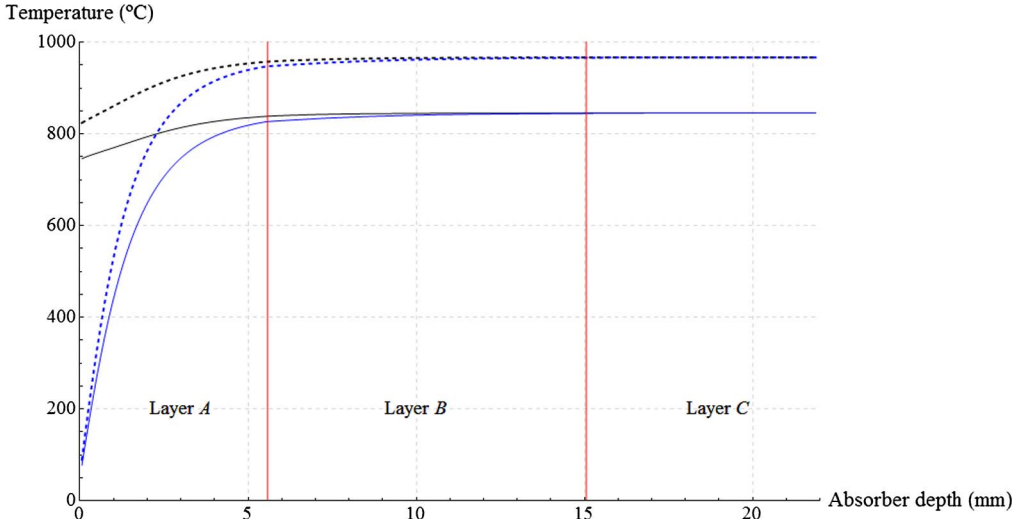

Fig. 32. Foam (black) and fluid (blue) temperature profiles of best triple-layer configuration – 0.5 kg/s (dashed line), 0.6 kg/s (solid line). (For interpretation of the references to colour in this figure legend, the reader is referred to the web version of this article.)

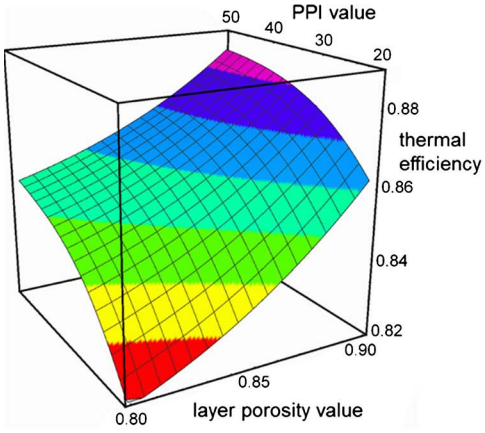

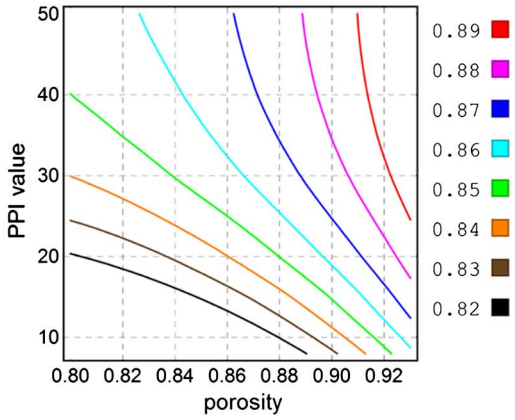

Fig. 33. Height (left) and contour (right) plot of absorber thermal efficiency vs porosity and PPI value for a single layer absorber (h = 60 mm) from the parameter variation analysis. Color contour limits with $\Delta\eta = 0.01$ spacing. (For interpretation of the references to colour in this figure legend, the reader is referred to the web version of this article.)

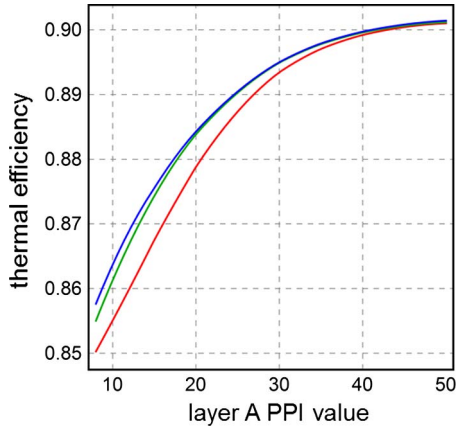

Fig. 34. Absorber thermal efficiency vs layer A PPI value for a dual layer absorber system. Layer B properties are assumed to $\epsilon_0 = 0.6$ and PPI 60. Results for $h_A = 10$ mm, $h_B = 50$ mm (red); $h_A = 20$ mm, $h_B = 40$ mm (green) and $h_A = 50$ mm, $h_B = 10$ mm (blue) are displayed. (For interpretation of the references to colour in this figure legend, the reader is referred to the web version of this article.)

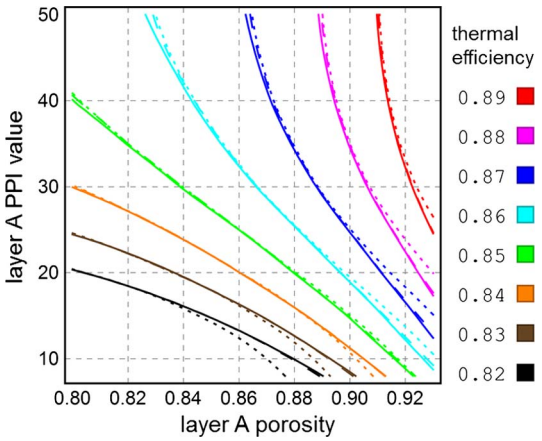

Fig. 35. Contour plot of absorber thermal efficiency vs layer A porosity and layer A PPI value for a dual layer absorber system. Layer B properties are assumed to $\epsilon_0 = 0.6$ and PPI 60 for a relatively dense layer. Results for $h_A = 10$ mm, $h_B = 50$ mm (dotted); $h_A = 20$ mm, $h_B = 40$ mm (dashed) and $h_A = 50$ mm, $h_B = 10$ mm (solid) are displayed.

sufficient. Additional layers do not contribute to thermal absorber performance but may be helpful to improve mechanical stability. Thus, all that again confirms the CENER model findings discussed in Section 5.1.

6. Conclusions

This work discusses two different 1-D numerical modeling approaches for ceramic foam volumetric solar absorbers, both considering local thermal non-equilibrium (LTNE) between fluid and solid phase along the modeling dimension (direction of air flow). The difference of the models lies in the modeling of radiation propagation inside the foam. One approach is based on a discrete-ordinate solution of the radiation transport equation; the other imposes the solar flux defining an exponential attenuation, as derived from Bouguer's law, and considering thermal radiation transport according to Rosseland's diffusion approximation.

Both numerical codes have been checked successfully for consistency against experimental data obtained at lab-scale solar simulator tests. Comparing the results of the DO model and the simplified one with imposed radiation, provided consistent trends and, in general, very similar results for all quantities. Nevertheless, the absolute level of the predicted air outlet temperature was significantly (20–50 K) lower for the simplified model in the analyzed cases. Providing a corrected effective reflectivity, a corrected effective foam emissivity and an effective emission temperature value obtained from averaging T^4 over the penetration depth zone (extension about 1/K) could improve the validity of the simplified model in future applications.

The following recommendation for an appropriate choice and application of the two model variants can be given:

- The DO model variant is well suited for detailed, locally resolved investigations of foam material parameter influences on volumetric absorber operation and performance due to its more realistic representation of the semitransparent character of the foam absorber.
- The simplified model with imposed radiation provides slightly different, but comparable results. Since it is implemented in Modelica code, it can be easily integrated into simulator applications on full system level, considering the interactions on solar receiver scale, the interactions with other components (heliostat field, heat exchangers, thermal energy storage, power conversion unit) and the dynamic behavior of the system. It nicely represents absorber integral characteristics and delivers a satisfying quantitative description in a full system simulation context.

Both models have been used for parametric studies optimizing for thermal efficiency. The optimization studies have shown that the porosity of the foam is strongly related to the obtained thermal efficiency. The higher the porosity of the foam is, the higher is also the obtained thermal efficiency. Thus, the highest possible porosity should be chosen for future solar receiver designs. A broad plateau-like efficiency maximum can be observed for cell densities between 30 and 50 PPI. When applying a multi-layer configuration, no significant correlation can be observed between efficiency and the properties of the second or third layer. Only the parameters of the first layer seem to determine the thermal performance. This leads to the conclusion that an optimized single-layer configuration is the absorber of choice. If necessary, a second layer could be applied to satisfy mechanical stability aspects. The absorber thickness has a rather weak influence on thermal performance; nevertheless, it develops an optimum between 10 and 30 mm. Thus, from the point of thermal performance only, the absorber thickness shall not be larger than 30 mm; thicknesses above 20 mm appear fully sufficient.

It has to be emphasized that these results are completely in line with the findings of Wu et al. [19], who concluded that in terms of thermal efficiency, a cell size of 1–2 mm (which is equal to the results of Fig. 22 of this work) combined with the highest possible level of porosity presents the most favorable choice for the solar absorber structure.

Acknowledgements

This work has received funding from the European Union's Horizon 2020 research and innovation program under the grant agreement No 640905.

References

[1] Abbott D. Keeping the energy debate clean: how do we supply the world's energy needs? Proc IEEE 2010;98:42–66.
[2] Kolb GJ. Evaluation of power production from the solar electric generating systems at Kramer Junction: 1988 to 1993. Albuquerque, New Mexico, USA: Sandia National Laboratories; 1994.
[3] Price H. Assessment of parabolic trough and power tower solar technology cost and performance forecasts. Golden, Colorado, USA: NREL – National Renewable Energy Laboratory; 2003.
[4] Reddy VS, Kaushik SC, Ranjan KR, Tyagi SK. State-of-the-art of solar thermal power plants – a review. Renew Sustain Energy Rev 2013;27:258–73.
[5] Solutia-Inc. Therminol VP-1 Heat Transfer Fluid by Solutia – Vapor Phase, Liquid Phase Heat Transfer Fluid (Technical Bulletin 7239115C). St. Louis, Missouri, USA: Solutia Inc.; 2008.
[6] Bradshaw RW, Carling RW. A review of the chemical and physical properties of molten alkali nitrate salts and their effect on materials used for solar central receivers – SAND87-8005 ed. Albuquerque New Mexico, USA: Sandia National Laboratories; 1987.
[7] Romero-Alvarez M, Zarza E, Kreith F, Goswami DY. Handbook of energy efficiency and renewable energy. Boca Raton, USA: CRC Press Taylor and Francis Group; 2007.
[8] Ávila-Marín AL. Volumetric receivers in solar thermal power plants with central receiver system technology: a review. Sol Energy 2011;85:891–910.
[9] Chavez JM, Chaza C. Testing of a porous ceramic absorber for a volumetric air receiver. Solar Energy Mater 1991;24:172–81.
[10] Fend T, Pitz-Paal R, Reutter O, Bauer J, Hoffschmidt B. Two novel high-porosity materials as volumetric receivers for concentrated solar radiation. Sol Energy Mater Sol Cells 2004;84:291–304.
[11] Fend T, Hoffschmidt B, Pitz-Paal R, Reutter O, Rietbrock P. Porous materials as open volumetric solar receivers: experimental determination of thermophysical and heat transfer properties. Energy 2004;29:823–33.
[12] Hoffschmidt B, Téllez FM, Valverde A, Fernández J, Fernández V. Performance evaluation of the 200-kWth HiTRec-II open volumetric air receiver. J SolEnergy Eng 2003;125:87–94.
[13] Téllez F. Thermal performance evaluation of the 200kWth "SolAir" volumetric solar receiver. Madrid, Spain: CIEMAT-PSA; 2003.
[14] Hennecke K, Hoffschmidt B, Koll G, Schwarzbözl P, Göttsche J, Beuter M, et al. The solar power tower Jülich – a solar thermal power plant for test and demonstration of air receiver technology. Presented at the ISES World Congress, Beijing, China; 2007.
[15] Heller P, Pfänder M, Denk T, Tellez F, Valverde A, Fernandez J, Ring A. Test and evaluation of a solar powered gas turbine system. Sol Energy 2006;80:1225–30.
[16] Grasse W. PHOEBUS: international 30 MWe solar tower plant. Solar Energy Mater 1991;24:82–94. 1991/12/02.
[17] Pitz-Paal R, Hoffschmidt B, Böhmer M, Becker M. Experimental and numerical evaluation of the performance and flow stability of different types of open volumetric absorbers under non-homogeneous irradiation. Sol Energy 1997;60:135–50.
[18] Bai F. One dimensional thermal analysis of silicon carbide ceramic foam used for solar air receiver. Int J Therm Sci 2010;49:2400–4.
[19] Wu Z, Caliot C, Flamant G, Wang Z. Coupled radiation and flow modeling in ceramic foam volumetric solar air receivers. Sol Energy 2011;85:2374–85.
[20] Modest M. Radiative heat transfer. 2nd ed. San Diego, USA: Academic Press – Elsevier Science; 2003.
[21] Wu Z, Wang Z. Fully coupled transient modeling of ceramic foam volumetric solar air receiver. Sol Energy 2013;89:122–33.
[22] Kribus A, Gray Y, Grijnevich M, Mittelman G, Mey-Cloutier S, Caliot C. The promise and challenge of solar volumetric absorbers. Sol Energy 2014;110:463–81.
[23] Mey-Cloutier S, Caliot C, Kribus A, Gray Y, Flamant G. Experimental study of ceramic foams used as high temperature volumetric solar absorber. Sol Energy 2016;136:226–35.
[24] Li Q, Bai F, Yang B, Wang Z, El Hefni B, Liu S, Kubo S, Kiriki H, Han M. Dynamic simulation and experimental validation of an open air receiver and a thermal energy storage system for solar thermal power plant. Appl Energy 2016;178:281–93.
[25] Hellmuth TE, Matthews LK, Chavez JM, Hale CA. Performance of a wire mesh solar volumetric air receiver, presented at the International Solar Energy Conference, San Francisco, California, USA; 1994.
[26] Hellmuth TE, Matthews LK. Experimental characterization of a high-temperature high-flux solar volumetric receiver. Exp Heat Transfer 1997;10:141–63.
[27] Hellmuth TE, Matthews LK. Modeling and optimum design of a wire mesh solar volumetric air receiver. J SolEnergy Eng 1997;119:208–13.
[28] Avila-Marin AL, Alvarez-Lara M, Fernandez-Reche J. Experimental results of gradual porosity wire mesh absorber for volumetric receivers. Energy Proc 2014;49:275–83.
[29] Ávila-Marín AL. Thermo-fluid-dynamic analysis of gradual porosity volumetric absorbers with metallic wire meshes: experimental study at lab-scale and numerical simulation with local thermal non-equilibrium model – PhD Thesis. Madrid: UNED; 2016.
[30] Roldán MI, Smirnova O, Fend T, Casas JL, Zarza E. Thermal analysis and design of a volumetric solar absorber depending on the porosity. Renew Energy 2014;62:116–28.
[31] Chen X, Xia X-L, Meng X-L, Dong X-H. Thermal performance analysis on a volumetric solar receiver with double-layer ceramic foam. Energy Convers Manage 2015;97:282–9.
[32] Richardson JT, Peng Y, Remue D. Properties of ceramic foam catalyst supports: pressure drop. Appl Catal A 2000;204:19–32.
[33] Adler J, Standke G. Offenzellige Schaumkeramik – Part 1. Keram Z 2003;55:694–703.
[34] Wu Z, Caliot C, Bai F, Flamant G, Wang Z, Zhang J, Tian C. Experimental and numerical studies of the pressure drop in ceramic foams for volumetric solar receiver applications. Appl Energy 2010;87:504–13.
[35] Inayat A, Freund H, Zeiser T, Schwieger W. Determining the specific surface area of ceramic foams: the tetrakaidecahedra model revisited. Chem Eng Sci 2011;66:1179–88.
[36] Wang F, Tan J, Yong S, Tan H, Chu S. Thermal performance analyses of porous media solar receiver with different irradiative transfer models. Int J Heat Mass Transfer 2014;78:7–16.
[37] Fend T, Schwarzbözl P, Smirnova O, Schöllgen D, Jakob C. Numerical investigation of flow and heat transfer in a volumetric solar receiver. Renew Energy 2013;60:655–61.
[38] Siegel R, Howell JR. Thermal radiation heat transfer – radiation transfer with absorbing emitting, and scattering Media. Washington, D.C.: NASA Special Publication; 1971. p. 164.
[39] Hendricks TJ, Howell JR. Absorption/scattering coefficients and scattering phase functions in reticulated porous ceramics. J Heat Transfer 1996;118:79–87.
[40] Schuetz MA, Glicksman LR. A basic study of heat transfer through foam insulation. J Cell Plast 1984;20:114–21.
[41] Xia X-L, Chen X, Sun C, Li Z-H, Liu B. Experiment on the convective heat transfer from airflow to skeleton in open-cell porous foams. Int J Heat Mass Transfer 2017;106:83–90.
[42] Endisch M. Experimentelle und numerische Untersuchungen zur stabilen Entsorgung von Schwachgasen in porösen Verbrennungsreaktoren – PhD Thesis, Freiberg, Germany: Technische Universität Bergakademie Freiberg; 2013.
[43] FCT-Keramik. Silicon carbide materials and components. Sonneberg, Germany: FCT Hartbearbeitungs GmbH; 2015.
[44] Becker M, Fend T, Hoffschmidt B, Pitz-Paal R, Reutter O, Stamatov V, et al. Theoretical and numerical investigation of flow stability in porous materials applied as volumetric solar receivers. Sol Energy 2006;80:1241–8.
[45] Khodaei H, Al-Abdeli YM, Guzzomi F, Yeoh GH. An overview of processes and considerations in the modelling of fixed-bed biomass combustion. Energy 2015;88:946–72.
[46] Bryden KM, Ragland KW, Rutland CJ. Modeling thermally thick pyrolysis of wood. Biomass Bioenergy 2002;22:41–53.
[47] Wessling S, Kessels W, Schmidt M, Krause U. Investigating dynamic underground coal fires by means of numerical simulation. Geophys J Int 2008;172:439–54.
[48] Sharma AK. Modeling fluid and heat transport in the reactive, porous bed of downdraft (biomass) gasifier. Int J Heat Fluid Flow 2007;28:1518–30.
[49] Kruesi M, Jovanovic ZR, Haselbacher A, Steinfeld A. Analysis of solar-driven gasification of biochar trickling through an interconnected porous structure. AIChE J

2015;61:867–79.
[50] Zhao CY, Lu TJ, Hodson HP. Thermal radiation in ultralight metal foams with open cells. Int J Heat Mass Transfer 2004;47:2927–39.
[51] Dietrich B, Fischedick T, Heissler S, Weidler PG, Wöll C, Kind M. Optical parameters for characterization of thermal radiation in ceramic sponges – experimental results and correlation. Int J Heat Mass Transfer 2014;79:655–65.
[52] Kreith F, Manglik RM, Bohn MS. Principles of heat transfer. Stamford, USA: Cengage Learning; 2011.
[53] Tummescheit H. Design and Implementation of Object-Oriented Model Libraries using Modelica, PhD Thesis ,Lund, Sweden: Department of Automatic Control - Lund Institute of Technology; 2002.
[54] McBride BJ, Zehe MJ, Gordon S. NASA Glenn coefficients for calculating thermodynamic properties of individual species. Cleveland, Ohio, USA: Glenn Research Center; 2002.
[55] Kadoya K, Matsunaga N, Nagashima A. Viscosity and thermal conductivity of dry air in the gaseous phase. J Phys Chem Ref Data 1985;14:947–70.
[56] Dietrich B. Heat transfer coefficients for solid ceramic sponges – experimental results and correlation. Int J Heat Mass Transfer 2013;61:627–37.
[57] Dietrich B, Schabel W, Kind M, Martin H. Pressure drop measurements of ceramic sponges—determining the hydraulic diameter. Chem Eng Sci 2009;64:3633–40.
[58] Holdich RG. Fundamentals of particle technology. Shepshed, Leicestershire, UK: Midland Information Technology and Publishing; 2002.
[59] Pitz-Paal R, Morhenne J, Fiebig M. A new concept of a selective solar receiver for high temperature applications. Solar Energy Mater 1991;24:293–306.
[60] Elmqvist H, Mattsson SE. Modelica – the next generation modeling language – an international design effort. Presented at the Proceedings of the 1st World Congress on System Simulation, Singapore; 1997.
[61] Modelica-Association. Modelica Standard Library 3.2 – Free library from the Modelica Association to model mechanical (1D/3D), electrical (analog, digital, machines), thermal, fluid, control systems and hierarchical state machines, " < http://www.modelica.org > (accessed 14.11.2012): Modelica-Association; 2010.
[62] Petzold LR. A description of DASSL: a differential/algebraic system solver. Albuquerque, New Mexico, USA: Sandia National Laboratories; 1982.
[63] Brenan KE, Campbell SL, Petzold LR. Numerical solution of initial-value problems in differential-algebraic equations. Philadelphia, USA: SIAM – Society for Industrial and Applied Mathematics; 1996.
[64] Nelder JA, Mead R. A simplex method for function minimization. Comput J 1965;7:308–13.